JGR Biogeosciences

RESEARCH ARTICLE
10.1029/2022JG007243

Key Points:

- The majority of models underestimate pCO_2 IAV, while they overestimate sea surface temperature IAV
- The ratio of non-thermal-to-thermal pCO_2 IAV is systematically underestimated in models, which results in weak total pCO_2 IAV
- Vertical dissolved inorganic carbon gradients are biased weak more than temperature gradients, but this alone doesn't explain the relative sizes of pCO_2 components

Supporting Information:

Supporting Information may be found in the online version of this article.

Correspondence to:

S. C. K. Wong,
suki.wong@columbia.edu

Citation:

Wong, S. C. K., McKinley, G. A., & Seager, R. (2022). Equatorial Pacific pCO_2 interannual variability in CMIP6 models. *Journal of Geophysical Research: Biogeosciences*, *127*, e2022JG007243. https://doi.org/10.1029/2022JG007243

Received 12 OCT 2022
Accepted 7 DEC 2022

Equatorial Pacific pCO_2 Interannual Variability in CMIP6 Models

Suki C. K. Wong[1], Galen A. McKinley[1], and Richard Seager[1]

[1]Department of Earth and Environmental Sciences, Lamont-Doherty Earth Observatory of Columbia University, Palisades, NY, USA

Abstract The El Niño-Southern Oscillation (ENSO) in the equatorial Pacific is the dominant mode of global air-sea carbon dioxide (CO_2) flux interannual variability (IAV). Air-sea CO_2 fluxes are driven by the difference between atmospheric and surface ocean pCO_2, with variability of the latter driving flux variability. Previous studies found that models in Coupled Model Intercomparison Project Phase 5 (CMIP5) failed to reproduce the observed ENSO-related pattern of CO_2 fluxes and had weak pCO_2 IAV, which were explained by both weak upwelling IAV and weak mean vertical dissolved inorganic carbon (DIC) gradients. We assess whether the latest generation of CMIP6 models can reproduce equatorial Pacific pCO_2 IAV by validating models against observations-based data products. We decompose pCO_2 IAV into thermally and non-thermally driven anomalies to examine the balance between these competing anomalies, which explain the total pCO_2 IAV. The majority of CMIP6 models underestimate pCO_2 IAV, while they overestimate sea surface temperature IAV. Insufficient compensation of non-thermal pCO_2 to thermal pCO_2 IAV in models results in weak total pCO_2 IAV. We compare the relative strengths of the vertical transport of temperature and DIC and evaluate their contributions to thermal and non-thermal pCO_2 anomalies. Model-to-observations-based product comparisons reveal that modeled mean vertical DIC gradients are biased weak relative to their mean vertical temperature gradients, but upwelling acting on these gradients is insufficient to explain the relative magnitudes of thermal and non-thermal pCO_2 anomalies.

Plain Language Summary To date, the global ocean has been responsible for absorbing over a third of carbon dioxide (CO_2) emissions, slowing down the growth of atmospheric CO_2 levels which drives global warming. Of interest is the equatorial Pacific Ocean, which is the largest oceanic source of CO_2 to the atmosphere with large fluctuations that are apparent in the record of global atmospheric CO_2. To study the ocean's ability to absorb future CO_2 emissions, we need models of the Earth system that can accurately capture fluctuations in the equatorial Pacific. In this paper, we assess surface ocean CO_2 fluctuations in the equatorial Pacific in the latest generation of models and we examine their deviations from observations. Compared to observations, models underestimate surface ocean CO_2 fluctuations as a result of excessive cancellation between competing drivers of CO_2 change. We find that the vertical gradient of carbon in models is too weak, which through ocean circulation, would contribute to weak surface CO_2 fluctuations. However, this does not fully account for underestimations in surface CO_2 fluctuations. Other processes have a significant role in excessively canceling surface CO_2 concentrations and requires further research.

1. Introduction

Carbon dioxide (CO_2) in the atmosphere is the main driver of anthropogenic radiative forcing via the greenhouse effect. Natural sinks in the ocean and land are damping the atmospheric CO_2 growth rate. The latest assessment of the global carbon budget averaged over recent decades (1960–2020) estimates the airborne fraction of atmospheric CO_2 emissions to be about 45%, with the remainder of emissions partitioned among the ocean (25%) and land (30%) (Friedlingstein et al., 2022). However, uncertainties in quantifying aspects of the global carbon cycle result in an imbalance in the carbon budget, which is largely attributed to errors in land and ocean sink estimates (Friedlingstein et al., 2022). Constraining ocean interannual variability (IAV) will help to reduce uncertainty in land IAV.

The equatorial Pacific is the largest natural oceanic source of CO_2 to the atmosphere (Takahashi et al., 2009), as a result of wind-driven upwelling in the region; upwelling brings cool waters that are rich in dissolved inorganic carbon (DIC) to the surface, which increases the partial pressure of CO_2 in the surface ocean (pCO_2). CO_2 outgassing IAV in the equatorial Pacific is dominated by the El Niño-Southern Oscillation (ENSO), and is

the dominant mode of global ocean sink IAV (Rödenbeck et al., 2014). ENSO mechanisms of air-sea CO_2 flux (FCO_2) variability are well understood. During an ENSO warm phase (El Niño), slackening trade winds over the equator reduces upwelling and brings about warm sea surface temperature (SST) anomalies (Bjerknes, 1966). Warm SST anomalies increase pCO_2 via reduced CO_2 solubility. However, it is the reduction in surface DIC due to reduced upwelling that dominates the CO_2 response (reduced CO_2 outgassing) during an El Niño (McKinley et al., 2004). During an ENSO cold phase (La Niña), the opposite happens and CO_2 outgassing is enhanced.

In Coupled Model Intercomparison Project Phase 5 (CMIP5), atmosphere-ocean global climate models were coupled with biogeochemical processes for the first time in CMIP history, allowing for carbon cycling in models (Emori et al., 2016; Taylor et al., 2012). Studies have reported biases in simulated equatorial Pacific pCO_2 and FCO_2 IAV in CMIP5 models, where weak surface DIC variability was found to be a source of bias in some models (Dong et al., 2017; Jin et al., 2019). Given ongoing climate change, there is a need for Earth System Models (ESMs) to make accurate climate projections. The latest generation of ESMs from CMIP6 have demonstrated progress in representing the mean state of ocean biogeochemistry (Séférian et al., 2020). However, as in CMIP5, weak FCO_2 IAV were also found in CMIP6 (Vaittinada Ayar et al., 2022). Identifying sources of model biases in FCO_2 IAV for the contemporary period, where some data constraints exist, is a first step toward model improvements.

Here, we assess equatorial Pacific pCO_2 IAV in 18 CMIP6 models over recent decades, comparing amplitudes and spatial patterns of variability against state-of-the-art observations-based pCO_2 products that span over five decades. We also compare the covariability of ENSO-related variables, such as SSTs, vertical velocity at 50 m (w_{50}), and thermocline depths with pCO_2 anomalies across the CMIP6 subset through lagged correlations. To understand biases in pCO_2 IAV, we decompose pCO_2 IAV into thermally (SST) and non-thermally (DIC, alkalinity and salinity) driven components. Imbalances between these competing components provide insight on biases in the total pCO_2 IAV.

In the equatorial Pacific, surface DIC variability dominates pCO_2 variability (Doney et al., 2009). Though there are several processes that drive DIC variability (FCO_2, freshwater fluxes, biology, vertical and horizontal transport), studies show that variability in the vertical transport of DIC is important to the overall budget of pCO_2 variability in the equatorial Pacific Ocean (Liao et al., 2020). Including temperature-driven pCO_2 variability, Liao et al. (2020) showed that the vertical transport term contributed the largest amount in their full mixed-layer pCO_2 budget decomposition (accounting for about 40% of the pCO_2 response; FCO_2 ~20%; biology ~18%; FW ~11%; horizontal transport ~10%; thermal and residual <1%). This demonstrated importance of the vertical transport of DIC in the equatorial Pacific motivates our investigation of its variability in CMIP6. There is also reason to believe that models are biased in mean vertical gradients (Farneti et al., 2022; Li & Xie, 2012), which through upwelling, could contribute to biases in surface DIC variability.

Our objectives are as follows: (a) compare equatorial Pacific pCO_2 IAV in CMIP6 models against observations-based data products, (b) understand why models underestimate pCO_2 IAV, and (c) identify sources of bias in the vertical transport of DIC in models. Given biases in mean vertical gradients of DIC and temperature, we quantify the degree to which upwelling anomalies (acting on biased gradients) contribute to the relative magnitudes of non-thermal and thermal pCO_2 IAV, respectively. Such assessment is necessary to ground work on how future changes in the variability and mean state of the tropical Pacific atmosphere-ocean system will also impact variability and shifts in air-sea CO_2 fluxes, with potential climate impact.

2. Models, Data and Methods

2.1. Models

Outputs from historical simulations (1959–2014) from 18 CMIP6 models (Table 1) are from the Pangeo cloud (http://pangeo.io), which were originally downloaded from the Earth System Grid Federation (ESGF)'s online archives (http://esgf-node.llnl.gov/projects/cmip6). We apply a data pre-processing Python tool to clean and unify data inconsistencies before any analysis (Busecke & Abernathey, 2020). We assess 18 models which have monthly pCO_2, FCO_2, SST, near-surface wind speeds measured at 10 m (u_{10}), ocean temperatures (T), w_{50} and DIC data available. Vertical velocities are calculated using the three-dimensional continuity equation for models that only have horizontal circulation data. For analyses that involve multiple ensemble members, ensemble members are chosen only if they have outputs for all the variables named above. This ensures that the internal variability,

Table 1
The Coupled Model Intercomparison Project Phase 6 (CMIP6) Models in This Assessment and Their References

Models	References
ACCESS-ESM1-5	Ziehn et al. (2019)
CanESM5	Swart et al. (2019a)
CanESM5-CanOE	Swart et al. (2019b)
CESM2	Danabasoglu (2019a)
CESM2-FV2	Danabasoglu (2019b)
CESM2-WACCM	Danabasoglu (2019c)
CESM2-WACCM-FV2	Danabasoglu (2019d)
CNRM-ESM2-1	Séférian (2018)
GFDL-CM4	Guo et al. (2018)
IPSL-CM6A-LR	Boucher et al. (2021)
MIROC-ES2L	Hajima et al. (2019)
MRI-ESM2-0	Yukimoto et al. (2019)
MPI-ESM1-2-LR	Wieners et al. (2019)
MPI-ESM1-2-HR	Jungclaus et al. (2019)
MPI-ESM-1-2-HAM	Neubauer et al. (2019)
NorESM2-LM	Seland et al. (2019)
NorESM2-MM	Bentsen et al. (2019)
UKESM1-0-LL	Byun (2020)

Note. For information about the ensemble members, see Table S1 in Supporting Information S1. Models in bold have a correct sign correlation between pCO_2 and vertical velocity and are assessed in all parts of this study.

unique to each run of a model (an ensemble member), is conserved across all output variables from a single run. For a list of the members that we use for each model, see Table S1 in Supporting Information S1.

2.2. Observations-Based Data Products

We use five out of the six available monthly gridded observations-based pCO_2 products from SeaFlux (Fay et al., 2021) for FCO_2 and surface ocean pCO_2 estimates. These five products include JENA-MLS, MPI-SOMFFN, CMEMS-FFN, JMA-MLR, and CSIR-ML6. We exclude a sixth product (NIES-FFNN) from our assessment as it was not able to recreate ENSO variability in pCO_2, such as the strong 1997–1998 El Niño event seen in the other products. For u_{10} data, we also use the three wind reanalysis products (CCMPv2, JRA55, and ERA5), used in SeaFlux to estimate fluxes.

DIC and total alkalinity (Alk) climatologies are from GLODAPv2 (Lauvset et al., 2021). GLODAPv2 is a mapped three-dimensional climatological data product of inorganic and carbon-related ocean variables. Observations of DIC and Alk are distributed in time too scarcely to allow determination of its time variation, so in GLODAPv2, the data have been averaged into a DIC climatology estimate. Monthly estimates of SST, ocean circulation and ocean temperature (1959–2014) are from a reanalysis product, ORAS5 of the European Center for Medium Range Weather Forecasts (Zuo et al., 2019). Unlike DIC and Alk, time variations can be resolved for SST, ocean circulation and ocean temperature variables in observations-based data products. We calculate vertical velocity using zonal and meridional ocean circulation data from ORAS5 via the vertical integration of the continuity equation. SST observations from another data set, HadISST (1959–2014; Rayner et al., 2003), are a secondary source for SST comparisons against models.

2.3. Methods

Model outputs are regridded to the same 1° × 1° longitude-latitude grid before any analysis. We define a region of the equatorial Pacific (5°N–5°S) between 180°E and 270°E, which encompasses the Niño 3 and 3.4 regions, extending 10° west of Niño 3.4, and refer to it as the Tropical Pacific Index (TPI) region. The Niño 3 and 3.4 regions are typically used to study the nature of ENSO variability over the equatorial Pacific Ocean, but here, the broader TPI region was chosen such that any longitudinal differences in the ENSO centers of action in models would be captured.

To compare relative amplitudes of IAV across models and other datasets, we use one standard deviation (σ) of detrended and deseasonalized monthly anomalies. Modeled FCO_2, pCO_2 and u_{10} IAV are compared against SeaFlux IAV. Note that historical simulations in CMIP6 models generate their own internal climate variability, and will not replicate the timings of historical events unless they are externally forced. Thus, when comparing SeaFlux IAV to model IAV, the temporal evolution is not expected to match. When calculating and comparing multi-year means between CMIP6 models and SeaFlux, data from the same time frame (1990–2014) are compared. This is done since multi-year means are sensitive to anthropogenic trends in CO_2; the ocean sink is changing over time in both observations-based data products and historical simulations, such that multi-year means are sensitive to the time frame over which the average is taken. The 1990–2014 time frame is chosen for multi-year means, because temporal coverage begins in 1990 for SeaFlux, and 2014 is the end year for CMIP6 historical simulations. Climatological monthly means taken over the study period are subtracted from monthly timeseries data to obtain deseasonalized monthly anomalies, and then, the data are detrended with the least squares method. In addition to model comparisons against SeaFlux, modeled SST IAV and vertical DIC gradients IAV are also compared against observations-based data products.

Spatial patterns of pCO_2 IAV are compared and assessed by calculating its first empirical orthogonal function (EOF) after detrending and deseasonalizing. EOF analyses are done on individual ensemble members that retain

full internal variability, and then averaged across ensemble members. The first principal components (PC1) and associated EOFs are all shown for the La Niña state (i.e., positive pCO_2 anomaly), as determined with reference to the sign of the TPI SST index. Model performances in reproducing IAV are assessed using spatial correlation coefficients (SCCs) between each model and observations-based pCO_2 patterns of IAV.

In order to examine the mechanisms of pCO_2 variability in models, local correlations between pCO_2 and SST anomalies within the tropical Pacific are calculated. Areas of strong correlations indicate regions in models where upwelling dominates pCO_2, which is consistent with the dominant ENSO signal. Lagged temporal correlations between pCO_2, SST, w_{50} and thermocline depth (z_{therm}) anomalies are also done to investigate the covariability of ENSO-related variables to pCO_2 anomalies. We define the z_{therm} as the depth of the maximum vertical temperature gradient. Time lags between variables are based on the lags seen in the observations-based data products: pCO_2 and SST are concurrently correlated, while w_{50} and z_{therm} anomalies lead pCO_2 by up to 3 months. Three-month running means of w_{50} and z_{therm} anomalies are taken before correlating them to the pCO_2 of the fourth month (e.g., the January-to-March mean of w_{50} anomalies are correlated to April's pCO_2 anomaly). pCO_2 is long-lived in the ocean, such that the influence of w_{50} and z_{therm} variability on local pCO_2 advects west due to mean currents during the 3 months of lag. To account for some of the westward advection of pCO_2 during the lag period, w_{50} and z_{therm} anomalies are calculated over a region 20° east of the TPI box region before correlating with pCO_2 anomalies over the TPI box region.

2.4. Thermal and Non-Thermal pCO_2 IAV

DIC, alkalinity (Alk) and salinity (S) are the non-thermal drivers of pCO_2 variability, while SST variability is the thermal driver. Thermal effects on pCO_2 typically oppose and dampen the non-thermal effects with ENSO (Sutton et al., 2014): for example, a reduction in upwelling brings less DIC to the surface which decreases surface pCO_2; simultaneously, the warmer SST anomalies, as a result of weakened upwelling, drives surface pCO_2 up via reduced solubility. We separate the non-thermally driven pCO_2 ($pCO_{2,nonT}$) from the thermally-driven counterpart ($pCO_{2,T}$) in order to explain modeled pCO_2 IAV. For $pCO_{2,nonT}$, temperature effects are removed by normalizing pCO_2 outputs to a long-term mean SST (Takahashi et al., 2002), following an empirical formulation determined by Takahashi et al. (1993):

$$pCO_{2,nonT} = pCO_2 \times e^{0.0423 \cdot \left(\overline{SST} - SST\right)}, \tag{1}$$

where $\overline{SST}$ is the multiyear mean of SST over time. The thermally driven component, $pCO_{2,T}$, is computed using the following equation (Takahashi et al., 2002):

$$pCO_{2,T} = \overline{pCO_2} \times e^{0.0423 \cdot \left(SST - \overline{SST}\right)}, \tag{2}$$

where $\overline{pCO_2}$ is the multiyear mean of pCO_2 during 1990–2014.

2.5. Vertical Transport of Dissolved Inorganic Carbon

Temporal changes in pCO_2 are a function of temporal changes in DIC, Alk, *S* and *T*, and can be expressed as the following linearly decomposed time derivative (Le Quéré et al., 2000; Liao et al., 2020; Takahashi et al., 1993):

$$\partial_t pCO_2 = \underbrace{\frac{\partial pCO_2}{\partial DIC}\partial_t DIC + \frac{\partial pCO_2}{\partial Alk}\partial_t Alk + \frac{\partial pCO_2}{\partial S}\partial_t S}_{\text{non-thermal}} + \underbrace{\frac{\partial pCO_2}{\partial T}\partial_t T}_{\text{thermal}}, \tag{3}$$

where we use the notation ∂_t to denote a partial derivative with respect to time. Temporal changes in DIC, Alk and S drive $pCO_{2,nonT}$, while temporal changes in SST drive $pCO_{2,T}$.

In the tropical Pacific, DIC variability has been found to be the dominant driver of pCO_2 variability, compared to Alk, S and *T* drivers (Doney et al., 2009; Le Quéré et al., 2000). From model results, Liao et al. (2020) found that alkalinity-driven effects on pCO_2 can exceed DIC-driven effects during El Niño, though DIC effects generally dominate in the eastern equatorial Pacific. Other model studies confirm that DIC is the dominant term in

the region (Jin et al., 2019; Long et al., 2013). The time tendency of surface DIC (∂_tDIC) is controlled by several processes including horizontal (H) and vertical (V) ocean transport, FCO_2, biological processes (Bio) and FW:

$$\partial_t \mathrm{DIC} \approx \partial_t \mathrm{DIC_H} + \partial_t \mathrm{DIC_V} + \partial_t \mathrm{DIC_{FCO_2}} + \partial_t \mathrm{DIC_{Bio}} + \partial_t \mathrm{DIC_{FW}} \tag{4}$$

Liao et al. (2020) showed that though other processes are non-negligible, vertical transport contributed the largest effect on pCO_2 change, with important vertical contributions from alkalinity and DIC in the model composite response. They also showed that the other processes are sensitive to changes in vertical transport: an increase in upwelling (increased surface DIC) drives an air-sea flux response, which damps surface DIC; upwelled nutrient-rich waters increase biological activity causing an increased uptake of DIC, which again damps surface DIC; and the horizontal transport of increased surface DIC results in a diverging transport, also damping. For CMIP5 models, Jin et al. (2019) showed that the vertical transport of DIC to the surface ocean overwhelms over other processes in reducing pCO_2 during an El Niño. In this study, we assess only the variability in vertical transport of DIC ($\partial_t \mathrm{DIC}_V$).

In order to quantify the contribution of the vertical transport of DIC ($\partial_t \mathrm{DIC}_V$) to $pCO_{2,nonT}$ variability ($\partial_t pCO_{2,\mathrm{nonT}}$), we evaluate the former in the same units as the latter—in units of the time tendency of pCO_2 (μatms^{-1})—and write $\partial_t \mathrm{DIC}_V$ as $w_{50}\partial_z \mathrm{DIC}$. Using coefficients from Equation 3, we can get both terms into the same units:

$$\frac{\partial pCO_2}{\partial \mathrm{DIC}} w_{50} \partial_z \mathrm{DIC} \qquad \left[\mathrm{units}: \mu\mathrm{atm}\ s^{-1}\right] \tag{5}$$

$$\partial_t pCO_{2,nonT} \qquad \left[\mathrm{units}: \mu\mathrm{atm}\ s^{-1}\right] \tag{6}$$

The coefficients used for the pCO_2 dependence on DIC are approximated as follows (Lovenduski et al., 2007):

$$\frac{\partial pCO_2}{\partial \mathrm{DIC}} \approx \frac{\overline{pCO_2}}{\overline{\mathrm{DIC}}} \cdot \frac{3 \times \overline{\mathrm{Alk}} \times \overline{\mathrm{DIC}} - 2 \times \overline{\mathrm{DIC}}^2}{\left(2 \times \overline{\mathrm{DIC}} - \overline{\mathrm{Alk}}\right)\left(\overline{\mathrm{Alk}} - \overline{\mathrm{DIC}}\right)}, \tag{7}$$

which can be expressed more simply as:

$$\frac{\partial pCO_2}{\partial \mathrm{DIC}} \approx \frac{\overline{pCO_2}}{\overline{\mathrm{DIC}}} \cdot \gamma_{\mathrm{DIC}}, \tag{8}$$

where γ_{DIC} is the buffer factor (Sarmiento & Gruber, 2006).

2.6. Reynolds' Decomposition

Using Reynolds' decomposition, we can separate the mean and the time-varying component:

$$w_{50} = \overline{w_{50}} + w'_{50}, \text{ and} \tag{9}$$

$$\partial_z \mathrm{DIC} = \partial_z \overline{\mathrm{DIC}} + \partial_z \mathrm{DIC}', \tag{10}$$

where primes denote detrended monthly anomalies and overbars denote long-term means. The time-varying component of the vertical transport of DIC, $\frac{\partial pCO_2}{\partial DIC}(w_{50}\partial_z \mathrm{DIC})'$, can be decomposed into three Reynold's terms:

$$\begin{aligned}\frac{\partial pCO_2}{\partial DIC}(w_{50}\partial_z \mathrm{DIC})' &= \frac{\partial pCO_2}{\partial DIC}\left(w_{50}\partial_z \mathrm{DIC} - \overline{w_{50}\partial_z \mathrm{DIC}}\right) \\ &= \frac{\partial pCO_2}{\partial DIC}\left(\underbrace{\overline{w_{50}}\partial_z \mathrm{DIC}'}_{\text{1st term}} + \underbrace{w'_{50}\overline{\partial_z \mathrm{DIC}}}_{\text{2nd term}}\right. \\ &\quad \left. + \underbrace{w'_{50}\partial_z \mathrm{DIC}' - \overline{w'_{50}\partial_z \mathrm{DIC}'}}_{\text{3rd term}}\right)\end{aligned} \tag{11}$$

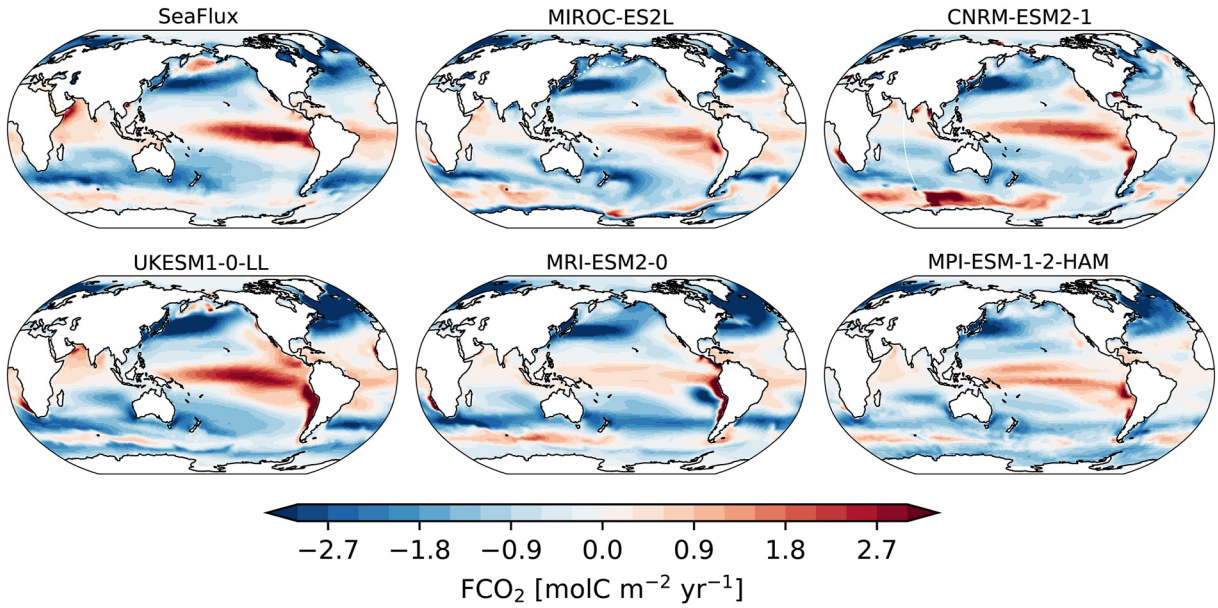

Figure 1. Multiyear mean maps of air-sea CO_2 flux (FCO_2 units: mol C m^{-2} yr^{-1}) taken over 1990–2014 for the SeaFlux ensemble-average, and five Coupled Model Intercomparison Project Phase 6 (CMIP6) models (one member was chosen per model): MIROC-ES2L, CNRM-ESM2-1, UKESM1-0-LL, MRI-ESM2-0, and MPI-ESM-1-2-HAM. Positive values (red) represent fluxes from the ocean to the atmosphere. Similar maps for all CMIP6 models are in Figure S1 in Supporting Information S1.

Note that the left-hand-side of Equation 11 is only the turbulent term of the vertical transport of DIC. For models, we compute all three Reynold's terms. In GLODAPv2, gridded DIC data are only available as a climatology. Since we can't calculate the time-varying vertical gradient of DIC, $\partial_z \mathrm{DIC}'$, we only compare the second Reynold's term $\left(\frac{\partial pCO_2}{\partial DIC} w'_{50} \partial_z \overline{\mathrm{DIC}}\right)$ between models and data.

3. Results

3.1. FCO_2 and pCO_2 Multiyear Means

A large region of FCO_2 outgassing can be seen in the equatorial Pacific Ocean, with the highest (positive, red) values being in the eastern region in SeaFlux (Figure 1: top-left). Comparing mean fluxes, five models (MIROC-ES2L, CNRM-ESM2-0, UKESM1-0-LL, MRI-ESM2-0, and MPI-ESM-1-2-HAM) are shown in Figure 1. These five models are selected to represent the range of abilities of CMIP6 models to reproduce data. Similar maps for all the CMIP6 models are available in Figure S1 in Supporting Information S1. The models have similar patterns to SeaFlux to the first order, with a basin-wide outgassing feature seen over the equatorial Pacific region, and the largest values lying in the eastern region. Model mean fluxes in the equatorial Pacific are typically weaker than SeaFlux, with the exception of UKESM1-0-LL which has a mean magnitude closer to SeaFlux (the CESM2 family of models also have comparable mean FCO_2 values, Figure S1 in Supporting Information S1). The mean outgassing in the equatorial region is noticeably weaker in MRI-ESM2-0 than the other models, and the MPI models show a narrow band of near-zero flux at the equator in the middle of the broader equatorial outgassing pattern.

Multiyear mean maps of pCO_2, averaged over 1990–2014, are plotted for SeaFlux and the same five CMIP6 models (Figure 2; Figure S2 in Supporting Information S1: all models). A SCC over the TPI region is calculated between each model and SeaFlux to quantify the model skill at reproducing the mean pCO_2 pattern. Note that a high SCC score does not indicate that the magnitude of the mean maps are similar. Generally, the majority of models produce the high pCO_2 equatorial structure seen in SeaFlux, with a third of all 18 models having an SCC score above 0.8 (Figure S2 in Supporting Information S1). The largest pCO_2 values are seen off coastal Peru and Panama in SeaFlux, with exaggerated coastal values seen in some of the models (MRI-ESM2-0 and UKESM1-0-LL). Unlike SeaFlux, the high pCO_2 equatorial structure extends almost all the way across the basin

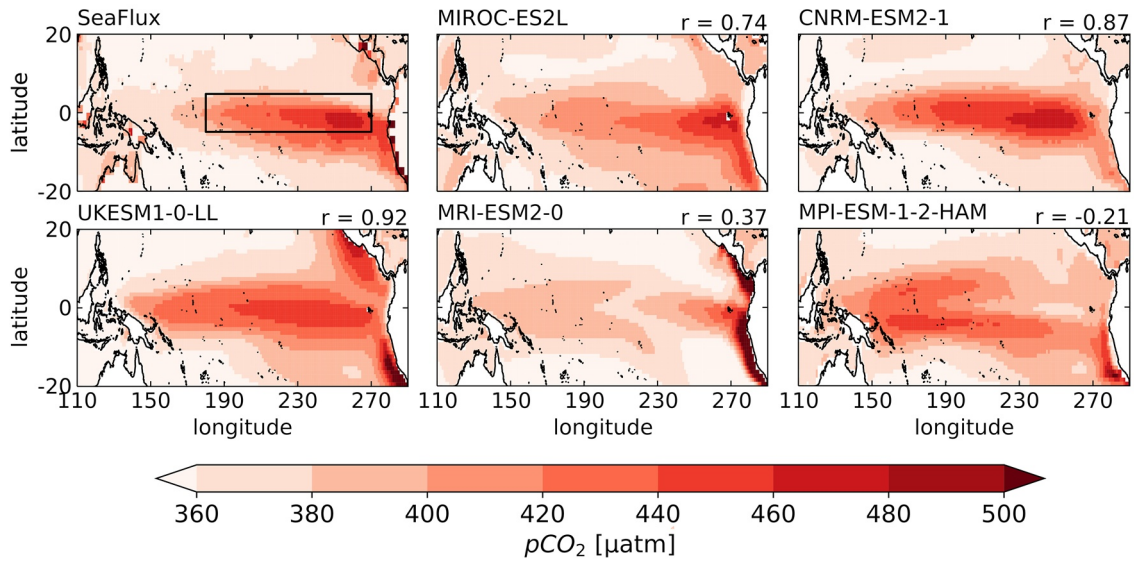

Figure 2. Tropical Pacific pCO_2 multi-year means from 1990 to 2014 (units: μatm) from the SeaFlux ensemble average (top-left) and five Coupled Model Intercomparison Project Phase 6 (CMIP6) models (other panels). The box in the SeaFlux panel marks the Tropical Pacific Index (TPI) region. The number (r) on the top right of each model's map is the spatial correlation coefficient between the model and SeaFlux in the TPI region. Model multi-year means are evaluated using a single ensemble member per model. Similar maps for all CMIP6 models are in Figure S2 in Supporting Information S1.

in the majority of models, except for the NorESM2 models (Figure S2 in Supporting Information S1). Similar to the FCO_2 multiyear mean maps, the MPI models show mean pCO_2 structures that exhibit an equatorial band of low pCO_2 that splits up the general high pCO_2 structure seen in SeaFlux and the other models.

3.2. Interannual Variability

The outgassing of CO_2 in the equatorial Pacific Ocean (Figure 1) is modulated by ENSO variability, which dominates the variability of global oceanic FCO_2 (Landschützer et al., 2016; McKinley et al., 2004, 2017; Rödenbeck et al., 2014). Amplitudes of FCO_2 IAV $\left(\sigma_{FCO_2'}\right)$ in the TPI region in CMIP6 differ from SeaFlux observations-based data products (Figure 3a). The majority of CMIP6 models underestimate FCO_2 IAV relative to SeaFlux over the TPI region with the exception of CESM2, CESM2-FV2, CNRM-ESM2-1 and MIROC-ES2L, which have members with FCO_2 IAV amplitudes that overlap with SeaFlux.

FCO_2 is a function of surface ocean and atmospheric pCO_2, and in the parameterization used in the models and data products, has a quadratic relationship to near-surface wind speeds, u_{10} (Wanninkhof, 2014). To investigate the underestimation of FCO_2 seen in CMIP6, we assess their amplitudes of pCO_2 and u_{10} IAV: $\sigma_{pCO_2'}$ and $\sigma_{u_{10}'}$, respectively (see Figures 3b and 3c). Similar to the FCO_2 IAV estimates, the majority of CMIP6 models underestimate pCO_2 IAV relative to SeaFlux. Meanwhile, u_{10} IAV is overestimated across the majority of models, with the exception of the CanESM5 models, the MPI models, and some smaller underestimation discrepancies from the GFDL-CM4 and MRI-ESM2-0 models, relative to three wind reanalysis data products. The underestimation in modeled pCO_2 IAV appears to be compensated by the overestimation in u_{10} IAV. In the MPI models, pCO_2 IAV is within range of data products, but FCO_2 is low due to low u_{10} IAV.

ENSO-driven variability has a concomitant effect on SST variability in the equatorial Pacific via the upwelling of cool waters. Figure 3d shows that the majority of CMIP6 models overestimate SST IAV in the TPI region, relative to ORAS5 and HadISST estimates. Models that underestimate pCO_2 IAV also overestimate SST IAV, with the exception of the CanESM5 models which underestimate both SST and pCO_2 IAV. Models also tend to overestimate u_{10} variance (Figures 3c and 3d). This is consistent with the coupling of wind speeds and SST variability via the Bjerknes feedback, where they amplify each other's anomalies.

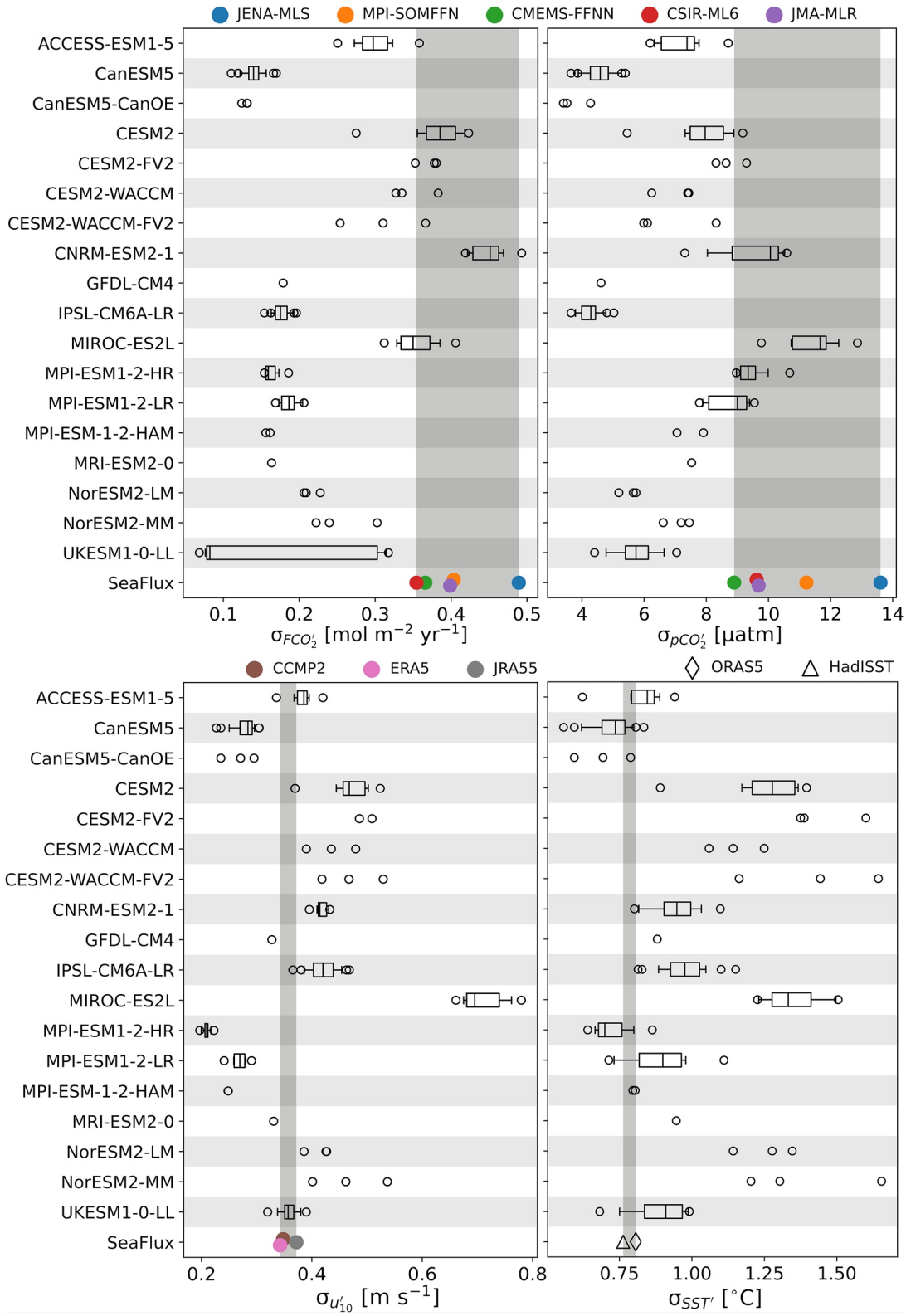

Figure 3. Comparison of IAV amplitudes in models (one standard deviation over the 1959–2014 period), and in observations-based data products (one standard deviation over the 1990–2014 period) in the Tropical Pacific Index region (5°N–5°S, 180°E–270°E). Top-left: FCO_2 IAV (units: mol C m^{-2} yr^{-1}); top-right: pCO_2 IAV (units: μatm); bottom-left: u_{10} IAV (units: $m\ s^{-1}$); bottom-right: Sea surface temperature IAV (units: °C). Boxplots represent the spread in IAV amplitudes within a model's ensemble members. For models where fewer than three members were available, the spread is shown without a boxplot. Observations-based data products are represented as the filled circles and the gray shaded regions indicate the range of IAV amplitudes within the observations-based data products.

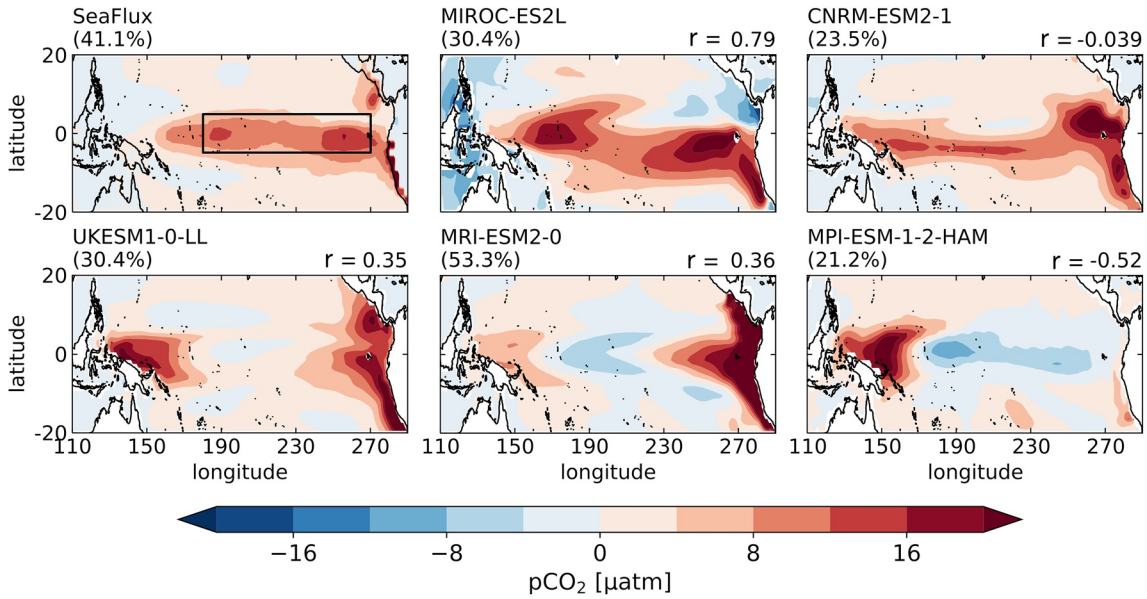

Figure 4. The first empirical orthogonal functions (EOFs) (units: μatm) of detrended pCO_2 anomalies in SeaFlux, averaged across the ensemble (top-left), and five Coupled Model Intercomparison Project Phase 6 (CMIP6) models (other panels). Model EOF patterns are calculated individually for each ensemble member before averaging over the ensemble. The percentage of the total variance in the tropical Pacific explained by EOF1 is given in parentheses above each panel. The number (r) on the top right of each model's panel is the spatial correlation coefficient over the Tropical Pacific Index (TPI) region between each model's EOF1 and SeaFlux's EOF1. The TPI region is shown by the box in the top-left panel. Similar maps for all CMIP6 models are in Figure S4 in Supporting Information S1. The corresponding principal components timeseries are shown in Figure S3 in Supporting Information S1.

3.3. Spatial Patterns of pCO_2 IAV

The EOF1 of SeaFlux (Figure 4: top-left) explains 41% of the total variance in pCO_2 IAV in the tropical Pacific, with a pattern that resembles that of ENSO variability of FCO_2 (McKinley et al., 2004; Resplandy et al., 2015). Its corresponding first PC1 is highly correlated with ORAS5 SST anomalies in the TPI region ($r = -0.82$, see Figure S3 in Supporting Information S1 for PC1 results), which indicates ENSO-driven variability in the tropical Pacific Ocean in the observations-based products.

In CMIP6, few models have an EOF1 that resembles the ENSO pattern seen in SeaFlux (Figure 4; Figure S4 in Supporting Information S1: all models). Further, models that have a realistic spatial pattern have too little variance in the first EOF mode. For example, MIROC-ES2L has an EOF1 pattern most similar to SeaFlux (SCC = 0.79), and explains 30% of the total pCO_2 variance. MIROC-ES2L, CNRM-ESM2-1 and UKESM1-0-LL reveal almost two-centers of action—near the coastlines on either side of the tropical Pacific—for pCO_2 variance. The weak correlation over the TPI region between SeaFlux and CNRM-ESM2-1 (SCC = −0.04) is because the positive pCO_2 variance in the model's EOF1 is shifted slightly south of the equator. MPI models show a "negative" EOF1 pattern, revealing pCO_2 variability that is opposite to what is expected from ENSO variability—that is, the pCO_2 and SST variability in its TPI region are positively correlated, in contrast to the negative correlation in SeaFlux.

Models that reproduce a realistic multiyear mean pCO_2 map (Figure 2), with respect to SeaFlux, do not necessarily have a realistic ENSO pattern of variability (Figure 4). Nevertheless, the relationship between PC1 and TPI SST anomalies do tend to be strong, with a median correlation of $r = -0.73$ (Figure S3 in Supporting Information S1). This is consistent with the ENSO signal where upwelling dominates pCO_2 variability (Feely et al., 2006; Sutton et al., 2014).

Figure 5 compares maps of the local correlation coefficient between pCO_2 and SST anomalies in models for the tropical Pacific. These correlations reveal the relative magnitude of $pCO_{2,T}$ and $pCO_{2,nonT}$ components of pCO_2 variability, since the dominance of either component will result in a correlation coefficient that is either positive (thermally dominant) or negative (non-thermally dominant). The strong, negative correlation pattern (blue areas) over the equatorial Pacific, seen in SeaFlux (Figure 5: top-left), indicates variability in upwelling of water that is both cool and DIC-rich with ENSO oscillations. Areas of positive correlations (red areas) indicate pCO_2 variability that is thermally driven; warmer SSTs drive higher pCO_2 levels. The negative pCO_2-SST relationship covers

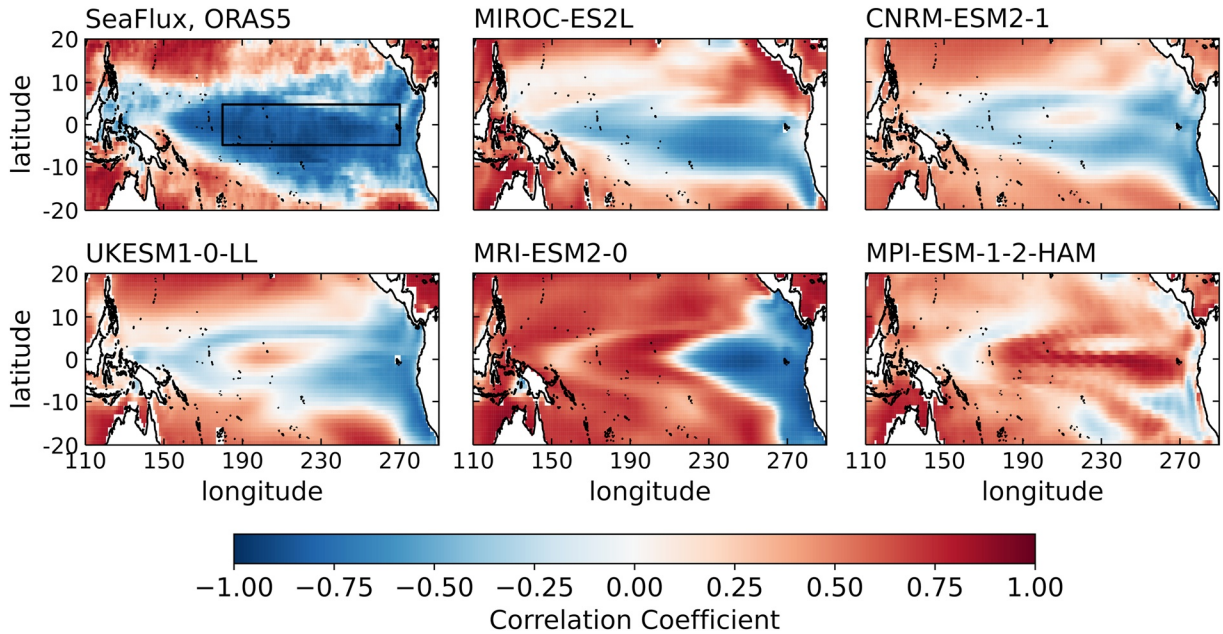

Figure 5. Correlation maps of detrended, pCO_2 and sea surface temperature monthly anomalies over the tropical Pacific region. Time periods used: 1990–2014 for SeaFlux and ORAS5 (top-left), and 1959–2014 for models (other panels). Model correlation maps were calculated individually for each ensemble member before averaging over the ensemble. For the observations-based map, the mean across SeaFlux pCO_2 products was first taken before correlating with ORAS5 SSTs. Maps for all models are in Figure S5 in Supporting Information S1.

a broad region in SeaFlux that spans the basin, with the strongest negative correlations at the equator. Compared to SeaFlux, MIROC-ES2L shows a pattern that covers a similar longitudinal span, however, the intensity of the negative correlations are not as strong, and does not extend as far north. MRI-ESM2-0 shows stronger correlations; however, its negative pattern does not cover the same longitudinal span as seen in SeaFlux. The lack of the negative pCO_2-to-SST extension to the west, common to most of the CMIP6 models, indicates that the ENSO-CO_2 co-variability lies more east in models than in SeaFlux. CNRM-ESM2-1, UKESM1-0-LL, MRI-ESM2-0 and MPI-ESM-1-2-HAM have a positive correlation zone within the Niño 3.4 region; CESM2 also has an anomalous positive correlation zone that lies more toward the east (Figure S5 in Supporting Information S1).

3.4. Thermal and Non-Thermal pCO_2 IAV

For SeaFlux and the CMIP6 models, detrended pCO_2 monthly anomalies decomposed into thermally ($pCO_{2,T}$) and non-thermally ($pCO_{2,nonT}$) driven anomalies (Equation 1 and 2) indicate the relative magnitudes of thermally and non-thermally driven pCO_2 variability (Figure 6: IPSL-CM6A-LR; S6: other models).

In SeaFlux, $pCO_{2,T}$ ($pCO_{2,nonT}$) anomalies are strongly, positively (negatively) correlated with SST anomalies, with correlation coefficients greater than 0.98. The total pCO_2 anomaly (Figure 6, bold black line) is strongly negatively correlated ($r = -0.92$) with TPI SST anomalies, due to the non-thermal component being dominant over the thermal component $\left(\sigma_{pCO'_{2,nonT}} > \sigma_{pCO'_{2,T}}\right)$.

In contrast, in IPSL-CM6A-LR (Figure 6: right), the non-thermal and thermal components have similar amplitudes but opposite sign $\left(\sigma_{pCO'_{2,nonT}} \sim \sigma_{pCO'_{2,T}}\right)$. This results in the total pCO_2 anomaly having almost no correlation ($r = -0.03$) with SST anomalies. $pCO_{2,T}$ variability almost completely counteracts $pCO_{2,nonT}$ variability, resulting in a weak total pCO_2 anomaly in IPSL-CM6A-LR. pCO_2 components in other CMIP6 models are also plotted (Figure S6 in Supporting Information S1). A summary plot of the relative amplitudes of the thermal and non-thermal components is shown in Figure 7.

Figure 7a compares the amplitudes of $pCO_{2,T}$ and $pCO_{2,nonT}$ anomalies across CMIP6 models' ensemble means. $\sigma pCO_{2,T}$ is 14.4 μatm for SeaFlux-ORAS5, and modeled values range from 11.5 to 25.3 μatm, with the multi-model

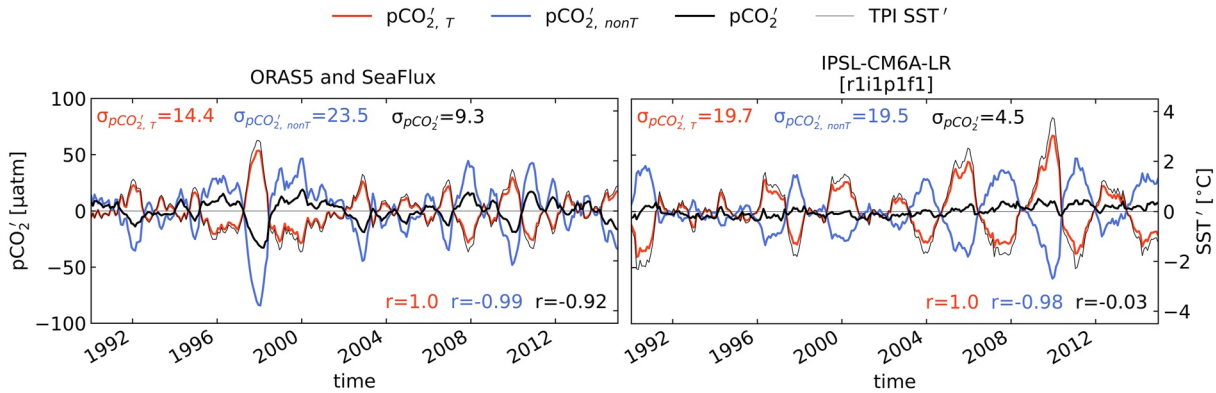

Figure 6. Timeseries of thermal ($pCO_{2,T}$; red), non-thermal ($pCO_{2,nonT}$; blue) and total pCO_2 anomalies (bold black) from an ensemble average of the SeaFlux products (left) and from a single member of IPSL-CM6A-LR (right); units: μatm. Thin black lines represent Tropical Pacific Index (TPI) sea surface temperature (SST) anomalies (units:°C; the SST *y*-axis is located on the right-hand-side). The top-left numbers in each panel are the IAV amplitudes (σ) of $pCO_{2,T}$, $pCO_{2,nonT}$, and total pCO_2 anomalies; the bottom-right numbers are their correlation coefficients (r) with TPI SST anomalies.

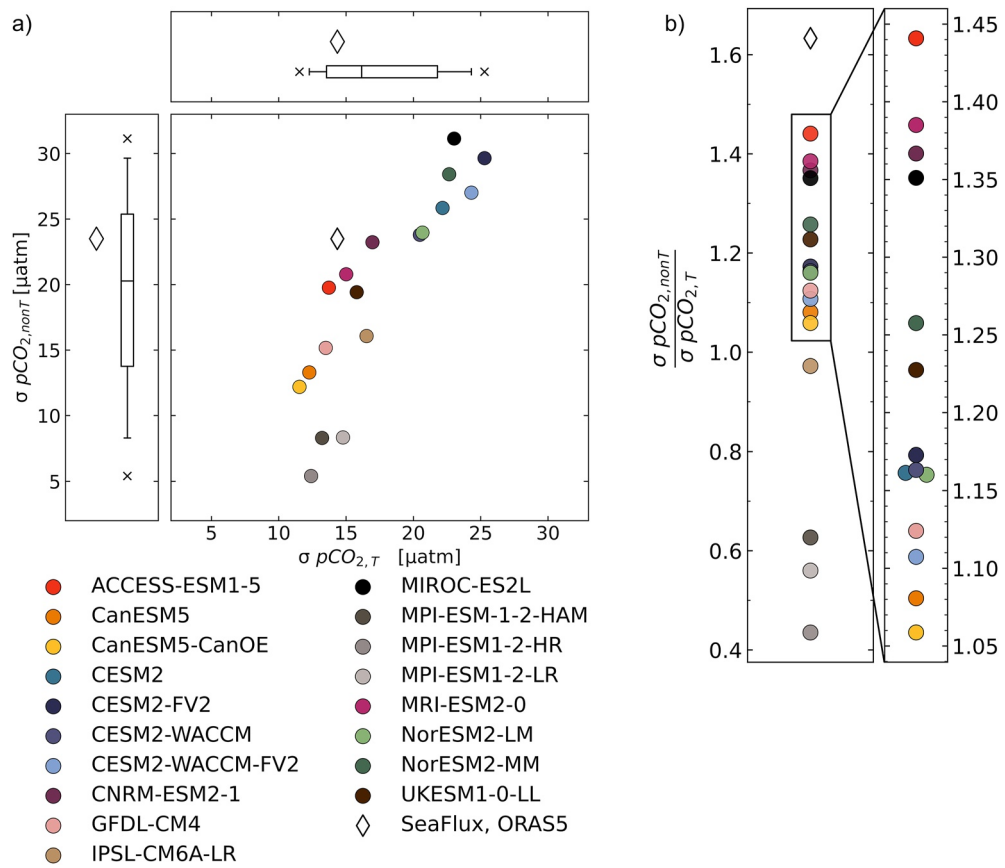

Figure 7. (a) Amplitudes of $pCO_{2,T}$ IAV (*x*-axis) versus $pCO_{2,nonT}$ IAV (*y*-axis) averaged over the Tropical Pacific Index region (units: μatm). Model ensemble means are represented by the filled circles, while the unfilled diamond represents the observations-based data products. Box plots around the figure show the distribution among models for $pCO_{2,T}$ and $pCO_{2,nonT}$ IAV amplitudes. (b) Ratios of $pCO_{2,nonT}$–$pCO_{2,T}$ IAV amplitudes in models (circles) and in the observations-based data products (diamond). Each scatter point represents the ensemble average for models and SeaFlux. The overlaid rectangle is magnified to see the models better.

median variance slightly higher than SeaFlux-ORAS5. On the other hand, $\sigma pCO_{2,nonT}$ for SeaFlux-ORAS5 is 23.5 μatm, while modeled $\sigma pCO_{2,nonT}$ ranges from 5.40 to 31.1 μatm with a multi-model median variance lower than that of SeaFlux-ORAS5. Figure 7b compares the ratios of $\sigma pCO_{2,nonT}$: $\sigma pCO_{2,T}$ in models against the ratio found in the observations-based data products; SeaFlux-ORAS5 has a ratio of 1.63, while the models all have smaller ratios, ranging from 1.44 (ACCESS-ESM1-5) to 0.44 (MPI-ESM1-2-HR). As such, compared to SeaFlux, modeled $\sigma pCO_{2,nonT}$ variability are not appropriately balanced against $\sigma pCO_{2,T}$. Models with a more dominant non-thermal component, that is, $\sigma pCO_{2,nonT}$: $\sigma pCO_{2,T}$ ratios closer to SeaFlux-ORAS5, have total pCO_2 anomalies that are more negatively correlated with TPI SST anomalies (Figure S6 in Supporting Information S1).

3.5. pCO_2 Correlations With Other Variables

We evaluate the co-variability of ENSO-related variables with pCO_2 in order to better understand the controls on $pCO_{2,T}$ and $pCO_{2,nonT}$ in models versus observations-based data products. Reduced upwelling brings less cool, DIC-rich water to the surface, resulting in warmer SSTs and reduced surface ocean pCO_2. The winds that drive upwelling also force z_{therm} anomalies; z_{therm} anomalies are positive (deeper) in the TPI region when the trades relax and upwelling weakens.

Correlations of SST, z_{therm}, and w_{50} anomalies with pCO_2 anomalies in the TPI region for SeaFlux are consistent with ENSO-driven variability as described above (Figure 8, clear diamonds; Figure S7 in Supporting Information S1), indicating that the observations-based products have realistic relationships between these variables and pCO_2, in particular with SST. For CMIP6, there is a large spread in correlations with pCO_2 (Figures 8a and 8b). NorESM2-MM and MIROC-ES2L have correlations similar to those seen in the observations-based data products. Models with incorrect correlation signs imply a lack of realistic relationships between these physical variables and pCO_2. For example, IPSL-CM6A-LR, and the MPI models have incorrect correlation signs between pCO_2 and the variables considered here.

Models that have more realistic correlation coefficients between pCO_2 and w_{50} or z_{therm} anomalies tend to do better at capturing the negative correlation between pCO_2 and SST anomalies (Figures 8a and 8b). The same models are better at representing $pCO_{2,nonT}$ variability (Figures 8c and 8d). Models with the weakest $pCO_{2,nonT}$ variances tend to be the same models with (a) weak or wrong-sign correlations (Figures 8a–8d), (b) lower non-thermal:thermal variance ratios (Figure 7; Figures 8c–8f), and (c) tend to do poorly in other areas throughout this assessment (Figures 2, 4, and 5). We leave out models that have incorrect correlation signs (negative) for pCO_2 and w_{50} anomalies (Figures 8b, 8d, and 8f) when looking at the vertical transport of DIC, since these models do not have realistic pCO_2-upwelling relationships (Table 1).

3.6. Vertical Ocean Transport of DIC

Despite having higher $pCO_{2,nonT}$ variances in the better performing models, the balances between the non-thermal and thermal components of pCO_2 variability are still not the same as seen in SeaFlux-ORAS5 (Figure 7b). The balance between these components are such that for a given magnitude of $pCO_{2,T}$ IAV, the relative magnitudes of $pCO_{2,nonT}$ IAV in models are insufficient to overwhelm it and produce the total pCO_2 IAV seen in SeaFlux. This motivates the rest of this assessment where we take a closer look at the vertical transport of DIC and its contribution to $pCO_{2,nonT}$ variability.

In Figure 9a, timeseries for each term in the Reynolds' decomposition (Equation 11) of the vertical transport of DIC in a single model (CESM2) are plotted against the time-tendency of $pCO_{2,nonT}\left(\partial_t pCO'_{2,nonT}\right)$. Figure 9b shows what can be obtained from data, which is just the second Reynolds term involving the climatological vertical DIC gradient and variable upwelling. With Reynolds' decomposition, we are able to isolate in models the contributions from variability in the vertical DIC gradient (Figure 9a: first panel) and the contributions from upwelling variability (Figure 9a: second panel) to $\partial_t pCO'_{2,nonT}$. The non-linear term (Figure 9a: third panel) is small. The fourth panel in Figure 9a compares the total anomaly of the vertical ocean transport of DIC against $\partial_t pCO'_{2,nonT}$. In CESM2, the first two Reynolds terms are roughly the same in magnitude, with standard deviations 2.65 and 2.77 times larger than the standard deviation of $\partial_t pCO_{2,nonT}$. The non-linear term is approximately the same magnitude as $\partial_t pCO_{2,nonT}$. The total anomaly (Figure 9a: fourth panel) has a standard deviation five times larger than the standard deviation of $\partial_t pCO'_{2,nonT}$, and has a positive correlation of $r = 0.70$. The magnitude of

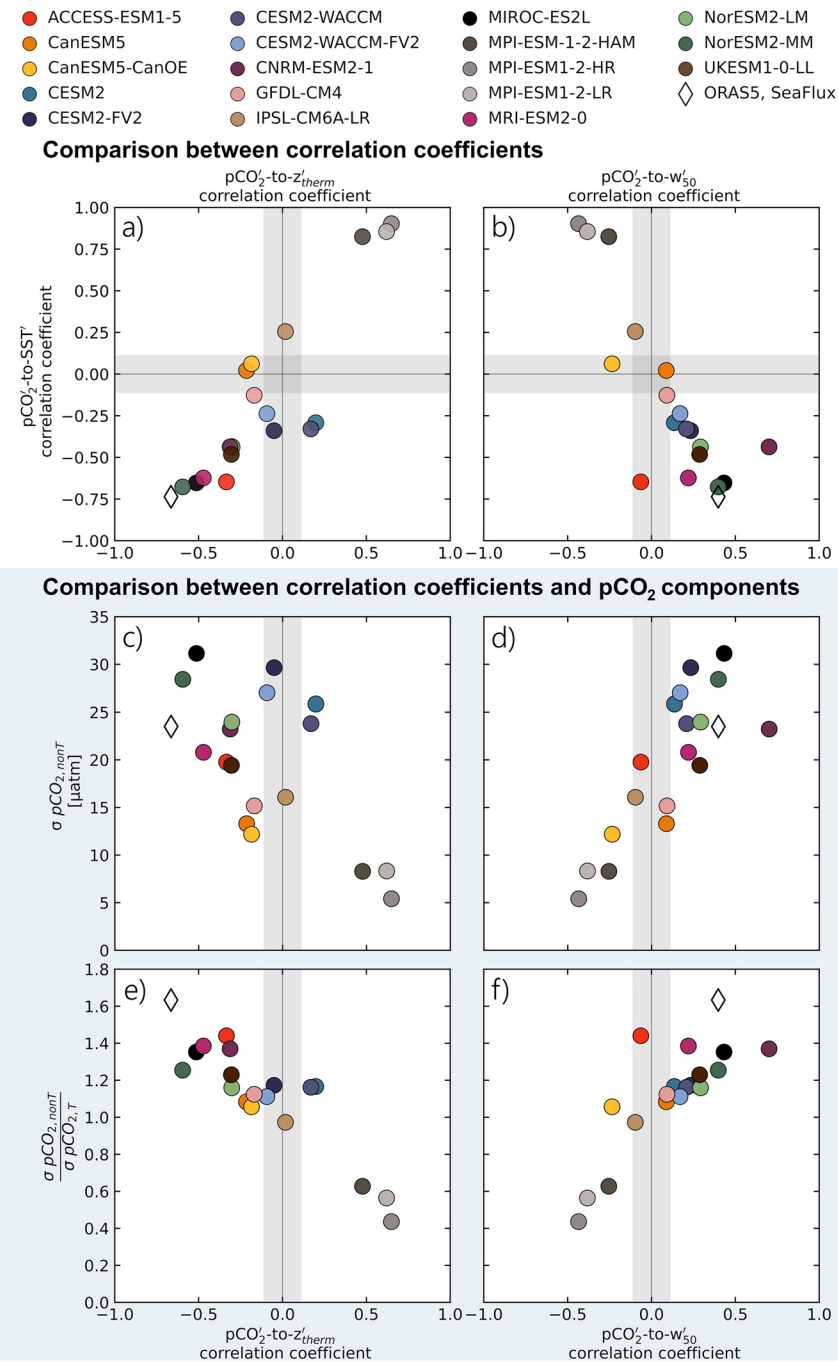

Figure 8. Scatter plot of the correlation coefficients of pCO_2'-to-z'_{therm} against (a) the correlation coefficients of pCO_2'-to-sea surface temperature', (c) $pCO_{2,nonT}$ variances, and (e) non-thermal:thermal variance ratios. Correlation coefficients are calculated over the Tropical Pacific Index region for the observations-based data products (clear diamonds), and the Coupled Model Intercomparison Project Phase 6 models (filled circles). The model correlation coefficients shown are ensemble means. The gray shading indicates the 95% confidence threshold for the correlations. Right-hand-side (b, d, f) is the same as the left-hand-side (a, c, e), but with pCO_2'-to-w'_{50} correlation coefficients along the *x*-axis instead.

the total anomaly in vertical DIC transport means that it is important to $pCO_{2,nonT}$ variability, and also that there must be strong damping terms. A summary of the Reynolds' terms in other models is in Table S2 in Supporting Information S1. Other models have similar results as CESM2 in that the total anomaly of vertical transport of DIC is significant in magnitude relative to the magnitude of $pCO_{2,nonT}$ variability. Values of their relative magnitudes,

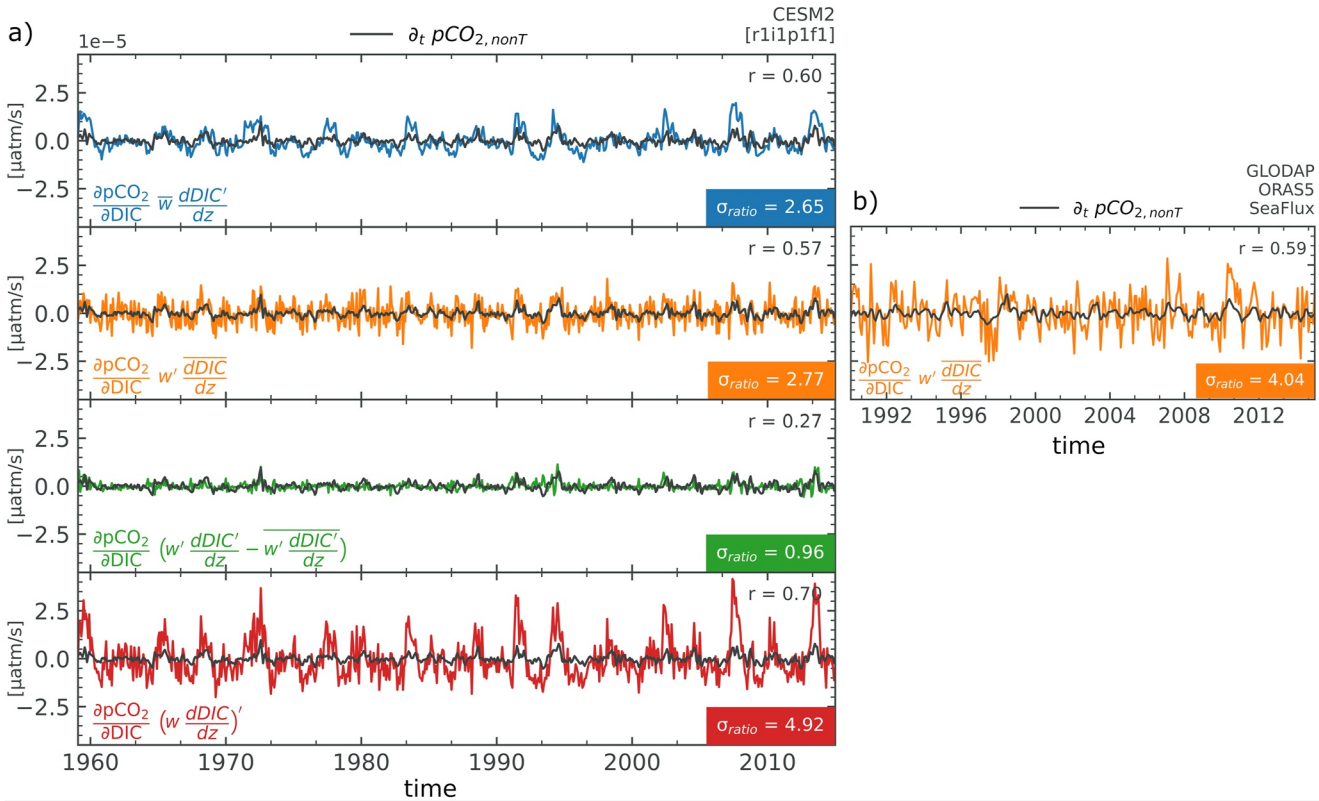

Figure 9. (a) Timeseries of the first (blue), second (orange) and third (green) Reynolds' terms from Equation 11, and the full variability is shown in the bottom panel (red) for one member from CESM2 (units: μatm s^{-1}). The time-tendency of $pCO_{2,nonT}$ is shown in every panel (black line). $\sigma_{\text{ratio}} = \sigma(\text{Reynolds' term})/\sigma\partial_t pCO_{2,nonT}'$ is annotated in every panel. The correlation coefficient (r) between the timeseries are also shown. For the other models, a summary of this information can be found in Table S2 in Supporting Information S1. (b) timeseries of the second Reynolds' term computed from observations-based data products.

σ_{ratio}, range from 2.94 to 5.55 (Table S2 in Supporting Information S1), which together with strong correlations, means that variability in the vertical transport of DIC is an important source of $pCO_{2,nonT}$ variability.

Across the models, the first two Reynolds' terms, $\overline{w_{50}}\partial_z DIC'$ and $w'_{50}\partial_z \overline{DIC}$, are the largest terms (Table S2 in Supporting Information S1), which suggests that the variability in both upwelling and vertical DIC gradients are similarly important to $pCO_{2,nonT}$ variability. In MIROC-ES2L, the non-linear term is almost the same amplitude as the first two terms. For observations-based data products, the second Reynolds term $\left(w'_{50}\partial_z \overline{DIC}\right)$ has a standard deviation four times bigger than the standard deviation of the observations-based $\partial_t pCO_{2,nonT}'$ (Figure 9b). Compared to the observations-based data products, the $w'_{50}\partial_z \overline{DIC}$ term is weak in models (Table S2 in Supporting Information S1, second column), except for UKESM1-0-LL. This could be due to either a weak vertical gradient of climatological DIC, or weak upwelling variability, or a combination of both.

A time-averaged vertical velocity section from ORAS5 (Figure S8a in Supporting Information S1) reveals that the depth at which upwelling occurs is within the upper 100 m, with a maxima between 50 and 75 m at 220°E. We compare upwelling variability in models versus ORAS5 in Figure 10a at 50 m. We find that the range of upwelling variability across models is comparable and inclusive of the upwelling variability seen in ORAS5. In contrast, Figure 10b compares the vertical gradient of climatological DIC at 50 m to GLODAPv2. All the models have weaker gradients. We repeat this comparison at 80 m (Figure S9 in Supporting Information S1) and confirm that it is robust. Modeled vertical gradients of climatological DIC are biased weak, causing the second Reynolds term $\left(w'_{50}\partial_z \overline{DIC}\right)$ in models to be weaker than the observations-based estimate (Figure 9; Table S2 in Supporting Information S1). To summarize, the second Reynold's term $\left(w'_{50}\partial_z \overline{DIC}\right)$ is an important term in the overall varia-

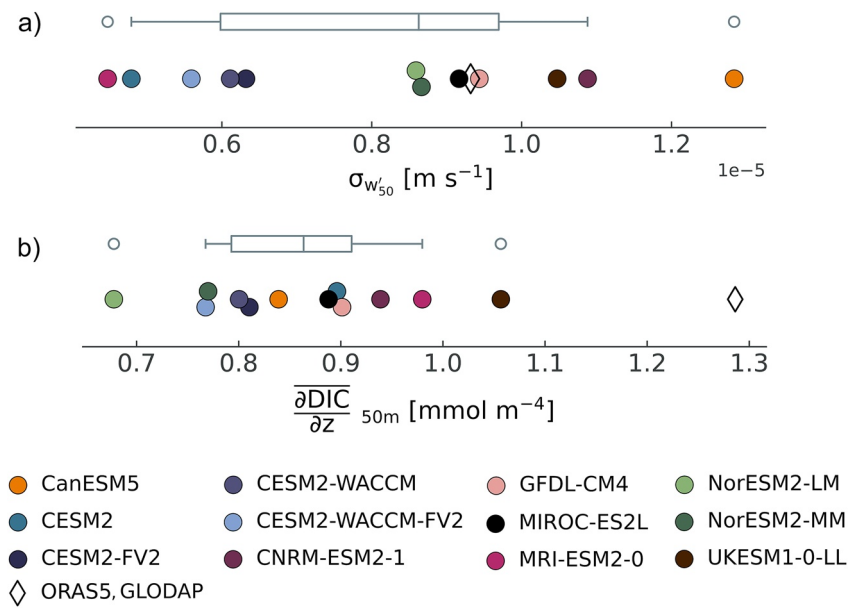

Figure 10. (a) Amplitudes (units: ms^{-1}) of upwelling IAV across models (filled circles are one member per model) versus ORAS5 (diamond). (b) Amplitudes (units: mmolm^{-4}) of vertical dissolved inorganic carbon gradients across models versus GLODAPv2. The boxplots represent the models only.

bility of the vertical transport of DIC, which is important to the variability in $pCO_{2,nonT}$, and thus pCO_2 variability. Underestimations in $w'_{50}\partial_z\overline{DIC}$ may result in an underestimation in pCO_2 variability.

Alongside modeled mean vertical DIC gradients, we plot the mean vertical temperature gradients $\left(\partial_z\overline{T}\right)$ at 50 m depth to compare the relative strengths of gradients in models, and to identify model biases from observations-based data products (Figure 11a). Vertical temperature gradients are negative since ocean temperatures decrease with depth. The spread in strengths of modeled temperature gradients encompasses that seen in ORAS5, though the majority of models have weaker temperature gradients. The percentage difference between ORAS5 and the models' median temperature gradient is about 21%. For the vertical gradient of climatological DIC, all models underestimate it compared to GLODAPv2, and the multi-model median has a percentage difference of about 39%. While the models tend to underestimate both the vertical gradients of climatological DIC and temperature, the climatological DIC gradients are more weakly biased, which for a given upwelling will tend to result in weaker $pCO_{2,nonT}$ variability relative to $pCO_{2,T}$.

The contributions of $w'_{50}\partial_z\overline{T}$ and $w'_{50}\partial_z\overline{DIC}$ in units of pCO_2 change (μatm) can be computed using the coefficients from Equation 7. Contributions from $w'_{50}\partial_z\overline{DIC}$ to pCO_2 in models are about 6 times greater than the thermal contributions (Figure 11b). The vertical DIC term is much bigger than the vertical T term, but the asscoiated $pCO_{2,nonT}$ variability is not proportionally bigger than $pCO_{2,T}$ variability (Figure 7). Thus, weak vertical gradients cannot fully explain the $pCO_{2,nonT}$-to-$pCO_{2,T}$ differences. Monthly pCO_2 variability (σpCO_2) in the TPI region in SeaFlux range from 8.9 to 13.6 µatm, and values in models range from 3.7 to 12.9 µatm (Figure 3). These values of monthly TPI pCO_2 variability are on the same order of magnitude as the $w'_{50}\partial_z\overline{DIC}$ contributions to pCO_2 (Figure 11b: y-axis). In observations, and in models, $w'_{50}\partial_z\overline{DIC}$ contributions to pCO_2 are larger than their monthly pCO_2 variability in the TPI region. Despite the large contributions from $w'_{50}\partial_z\overline{DIC}$ to pCO_2 variability, significant damping must be happening to reduce overall pCO_2 variability and cause its underestimation.

4. Discussion

The majority (15) of the 18 CMIP6 models underestimate pCO_2 IAV, while they overestimate SST IAV. FCO_2 IAV is also underestimated by the majority of CMIP6 models. Previous studies of historical simulations from the earlier CMIP5 found that FCO_2 IAV were also underestimated in models (Dong et al., 2016, 2017). Results from

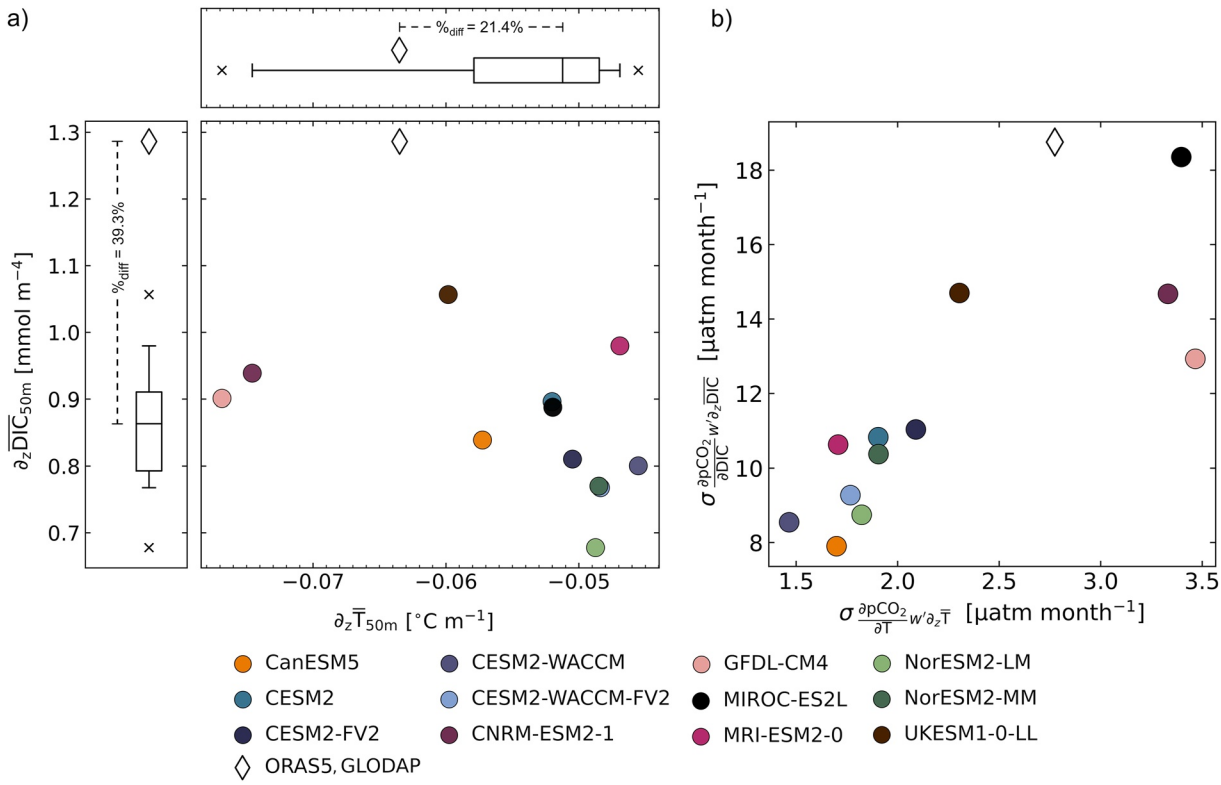

Figure 11. (a) The relative strength of vertical mean temperature gradients (*x*-axis, units: °Cm^{-1}) against vertical climatological dissolved inorganic carbon (DIC) gradients (*y*-axis, units: mmolm^{-4}) in models (filled circles represent a single ensemble member) and in ORAS5 versus GLODAPv2 data (clear diamond). The boxplots represent the distribution in gradients among models, excluding observations-based data products (clear diamonds). (b) The vertical transport of the climatological vertical temperature gradient versus the DIC gradient, converted from units of μatm s^{-1} into units of μatm month^{-1}.

another CMIP6 study also find that most models simulate weak FCO_2 anomalies while overestimating SST IAV (Vaittinada Ayar et al., 2022).

We find that the correlations between pCO_2 and other ENSO-related variables vary. Most models have correlations weaker than observed over the TPI region, a few are consistent with observations, and another few are opposite to observed. Weak ENSO-driven relationships were also noted in previous CMIP5 studies (Dong et al., 2017; Jin et al., 2019). Dong et al. (2016) also found that 12 models out of the 18 CMIP5 subset failed to show ENSO characteristics in FCO_2 variability. They also found that models differed among themselves the most in regions with strong vertical movement, such as the tropical Pacific.

Modeled $pCO_{2,nonT}$ variance in CMIP6 is not appropriately balanced with $pCO_{2,T}$ variability. Weak $pCO_{2,nonT}$ anomalies are insufficient to counteract the $pCO_{2,T}$ anomalies resulting in total pCO_2 anomalies that are too weak. In the equatorial Pacific, Jin et al. (2019) found pCO_2 biases in two CMIP5 models that resulted from weak DIC contributions to pCO_2. Weak DIC contributions were found to be mainly caused by weak vertical gradients of climatological DIC and weak upwelling anomalies, which both limit the vertical transport of DIC (Jin et al., 2019). We find that upwelling anomalies in CMIP6 are comparable to ORAS5 (Figure 10a).

Changes in the vertical transport of DIC affects surface DIC variability, which is known to be the dominant driver of pCO_2 variability in the surface equatorial Pacific Ocean (Liao et al., 2020; McKinley et al., 2004). We find model pCO_2 anomalies due to variability in the vertical transport of DIC are larger than their $pCO_{2,nonT}$ anomalies by a factor of 3 to almost 6 times (see Table S2 in Supporting Information S1: last column) but are positively correlated. This suggests that variability in the vertical transport of DIC is an important source of $pCO_{2,nonT}$ variability in models. At the same time, $w'_{50}\partial_z\overline{DIC}$ contributions to pCO_2 are comparable in magnitude to daily pCO_2 variability in the TPI region (Figure 11b). Together, these findings indicate that $w'_{50}\partial_z\overline{DIC}$ contributions to pCO_2 variability are significantly damped by other processes.

The vertical gradient of climatological DIC is consistently weak across all the models relative to observations-based data products (Figure 10), which is consistent with prior model results from CMIP5 (Jin et al., 2019). Vertical gradients of climatological temperature are not as weak. The imbalance in the relative strengths of these vertical gradients, for a given upwelling anomaly, contributes toward weaker non-thermal pCO_2 variability, relative to the thermal.

While the relative strengths of mean vertical gradients, through upwelling, can result in weaker $\sigma pCO_{2,nonT}$: $\sigma pCO_{2,T}$ ratios, we do not find a linear scaling between the relative strengths in mean vertical gradients and the ratios of $\sigma pCO_{2,nonT}$: $\sigma pCO_{2,T}$ across the models (Figure S10 in Supporting Information S1). A linear scaling would indicate that biases in the relative strengths of the mean vertical gradients proportionally bias the pCO_2 ratios. Thus, we find the relative strengths of mean vertical gradients alone do not determine the imbalance in pCO_2 ratios. A more complete assessment that includes the other processes that contribute to pCO_2 variability will be necessary to understand the causes of insufficient $pCO_{2,nonT}$ variability.

Other processes that contribute to equatorial Pacific DIC variability that can dampen $pCO_{2,nonT}$ variability, include the horizontal transport of DIC, biological processes, FW and air-sea CO_2 fluxes. For example, when DIC is bought to the surface via upwelling, though pCO_2 increases, the instantaneous air-sea CO_2 flux response dampens surface DIC concentrations (Liao et al., 2020). The biological response also damps surface DIC concentrations; upwelling of nutrient-rich waters enhances biologically-driven uptake of DIC (Chavez et al., 1999). Freshwater fluxes (rainfall) also dilute surface DIC concentrations, and westward horizontal transport along the equator removes DIC from the upwelling region (Doney et al., 2009).

Aside from DIC, other ocean biogeochemical variables influence surface $pCO_{2,nonT}$, such as alkalinity. We repeat our analysis for the vertical ocean transport of DIC with alkalinity data to evaluate how much surface alkalinity variability damps pCO_2 variability. We find that the contributions from $w'_{50}\partial_z\overline{Alk}$ damps $w'_{50}\partial_z\overline{DIC}$ contributions to pCO_2 anomalies by roughly 10% across models and observations-based data products (Figure S11 in Supporting Information S1). However, this amount of damping is not enough to explain the insufficient $pCO_{2,nonT}$ variability. Vaittinada Ayar et al. (2022) find that models with strong alkalinity biases have weak surface DIC biases (i.e., weak surface DIC variability), which leads to a reduction in $pCO_{2,nonT}$ variability. They find that for some models (CanESM5, GFDL-CM4 and MRI-ESM2-0), $pCO_{2,nonT}$ variability is weak enough that pCO_T variability can dominate total pCO_2 anomalies. However, an alkalinity bias alone does not explain all the models that underestimate $pCO_{2,nonT}$, relative to $pCO_{2,T}$, as we analyze here. For example, Vaittinada Ayar et al. (2022) shows that IPSL-CM6A-LR doesn't have a strong alkalinity bias, however, we find that its $pCO_{2,nonT}$: $pCO_{2,T}$ variance ratio is weaker than the ratio in MRI-ESM2-0 (Figure 7b), which is a model they show with a strong alkalinity bias.

Vaittinada Ayar et al. (2022) proposed that models without a strong alkalinity bias may be better predictors of future ENSO-CO_2 flux dynamics. However, we find that these models underestimate equatorial Pacific pCO_2 IAV and ENSO-related covariability. For example, IPSL-CM6A-LR did not have realistic correlations between pCO_2 and SST, z_{therm} or w_{50} anomalies (Figure 8b). We propose that a wide range of variables need to be considered when selecting models for analysis of future trends. While this study looks at ENSO-driven pCO_2 IAV, it has relevance for trends. Trends in SSTs, thermocline depths and upwelling in response to rising atmospheric CO_2 involve many of the same coupled dynamics that drive ENSO variability (Cane et al., 1997; Clement et al., 1996; Seager et al., 2019). CMIP6 models cannot reproduce the observed trends in the tropical Pacific physical state and hence it is possible that they are also misrepresenting the trends in pCO_2 and air-sea CO_2 fluxes, with potential influence on the airborne fraction of anthropogenic CO_2. Validating ENSO-driven pCO_2 variability in models is a necessary first step to examining the tropical Pacific's coupled climate-carbon response to anthropogenic climate change.

5. Conclusions

In the equatorial Pacific, weak ENSO-related pCO_2 variability in CMIP6 models is explained by an imbalance between $pCO_{2,nonT}$ and $pCO_{2,T}$ anomalies, whereby $pCO_{2,nonT}$ variability is insufficient to counteract strong $pCO_{2,T}$ variability. Strong $pCO_{2,T}$ variability in CMIP6 is driven by excessive SST variance. Variability in the vertical transport of DIC does matter to $pCO_{2,nonT}$ variability in that upwelling anomalies acting on weak vertical DIC gradients can lead to weaker surface DIC variability. However, this alone does not explain the relative magnitudes of $pCO_{2,nonT}$ and $pCO_{2,T}$ anomalies. To guide model development, assessments of other processes that drive DIC

variability will help to identify the causes of significant damping of $pCO_{2,nonT}$ variability that ultimately leads to weak pCO_2 variability in models.

Conflict of Interest

The authors declare no conflicts of interest relevant to this study.

Data Availability Statement

CMIP6 model output data are available at: http://esgf-node.llnl.gov/projects/cmip6. Information on installing and using the CMIP6 data pre-processing Python package (Busecke & Abernathey, 2020) can be accessed here: https://cmip6-preprocessing.readthedocs.io/en/latest/. SeaFlux products (including wind speed products) are available on Zenodo: https://doi.org/10.5281/zenodo.5482547. GLODAPv2.2021 data, archived at NOAA-NCEI at https://www.ncei.noaa.gov/access/metadata/landing-page/bin/iso?id=gov.noaa.nodc:0237935, can also be downloaded from the GLODAP website: https://www.glodap.info/. The ECMWF-ORAS5 data set can be downloaded from the Integrated Climate Data Center portal at http://icdc.cen.uni-hamburg.de/thredds/catalog/ftpthredds/EASYInit/oras5/catalog.html and https://www.cen.uni-hamburg.de/icdc/data/ocean/easy-init-ocean/ecmwf-oras5-backward-extension.html for 1979–2018 and 1958–1978, respectively. HadISST data were obtained from https://www.metoffice.gov.uk/hadobs/hadisst/ and are © British Crown Copyright, Met Office (2022), provided under a Non-Commercial Government License http://www.nationalarchives.gov.uk/doc/non-commercial-government-licence/version/2/.

Acknowledgments

We acknowledge the World Climate Research Programme, which, through its Working Group on Coupled Modeling, coordinated and promoted CMIP6. We thank the climate modeling groups for producing and making available their model output, the Earth System Grid Federation (ESGF) for archiving the data and providing access, and the multiple funding agencies who support CMIP6 and ESGF. SW acknowledges Pangeo for providing cloud-services for this research, and would also like to thank Julius Busecke for their CMIP6 pre-processing Python package. SW thanks the Columbia Graduate School of Arts and Sciences for funding. This research was supported in part by the National Science Foundation (OCE 22-19829, OCE-1948624, LEAP STC 2019625).

References

Bentsen, M., Oliviè, D. J. L., Seland, Y., Toniazzo, T., Gjermundsen, A., Graff, L. S., et al. (2019). NCC NorESM2-MM model output prepared for CMIP6 CMIP historical [Dataset]. Earth System Grid Federation. https://doi.org/10.22033/ESGF/CMIP6.8040

Bjerknes, J. (1966). A possible response of the atmospheric hadley circulation to equatorial anomalies of ocean temperature. *Tellus*, *18*(4), 820–829. https://doi.org/10.3402/tellusa.v18i4.9712

Boucher, O., Denvil, S., Levavasseur, G., Cozic, A., Caubel, A., Foujols, M.-A., et al. (2021). IPSL IPSL-CM6A-LR-INCA model output prepared for CMIP6 CMIP historical [Dataset]. Earth System Grid Federation. https://doi.org/10.22033/ESGF/CMIP6.13601

Busecke, J., & Abernathey, R. (2020). CMIP6 without the interpolation: Grid-native analysis with Pangeo in the cloud. *Earth and Space Science Open Archive*, *1*. https://doi.org/10.1002/essoar.10504242.1

Byun, Y.-H. (2020). NIMS-KMA UKESM1.0-LL model output prepared for CMIP6 CMIP historical [Dataset]. Earth System Grid Federation. https://doi.org/10.22033/ESGF/CMIP6.8379

Cane, M. A., Clement, A. C., Kaplan, A., Kushnir, Y., Pozdnyakov, D., Seager, R., et al. (1997). Twentieth-century sea surface temperature trends. *Science*, *275*(5302), 957–960. https://doi.org/10.1126/science.275.5302.957

Chavez, F. P., Strutton, P. G., Friederich, G. E., Feely, R. A., Feldman, G. C., Foley, D. G., & McPhaden, M. J. (1999). Biological and chemical response of the equatorial Pacific ocean to the 1997-1998 El Niño. *Science*, *286*(5447), 2126–2131. https://doi.org/10.1126/science.286.5447.2126

Clement, A. C., Seager, R., Cane, M. A., & Zebiak, S. E. (1996). An ocean dynamical thermostat. *Journal of Climate*, *9*(9), 2190–2196. https://doi.org/10.1175/1520-0442(1996)009⟨2190:AODT⟩2.0.CO;2

Danabasoglu, G. (2019a). NCAR CESM2 model output prepared for CMIP6 CMIP historical [Dataset]. Earth System Grid Federation. https://doi.org/10.22033/ESGF/CMIP6.7627

Danabasoglu, G. (2019b). NCAR CESM2-FV2 model output prepared for CMIP6 CMIP historical [Dataset]. Earth System Grid Federation. https://doi.org/10.22033/ESGF/CMIP6.11297

Danabasoglu, G. (2019c). NCAR CESM2-WACCM model output prepared for CMIP6 CMIP historical [Dataset]. Earth System Grid Federation. https://doi.org/10.22033/ESGF/CMIP6.10071

Danabasoglu, G. (2019d). NCAR CESM2-WACCM-FV2 model output prepared for CMIP6 CMIP historical [Dataset]. Earth System Grid Federation. https://doi.org/10.22033/ESGF/CMIP6.11298

Doney, S. C., Lima, I., Feely, R. A., Glover, D. M., Lindsay, K., Mahowald, N., et al. (2009). Mechanisms governing interannual variability in upper-ocean inorganic carbon system and air–sea CO_2 fluxes: Physical climate and atmospheric dust. *Deep Sea Research Part II: Topical Studies in Oceanography*, *56*(8), 640–655. (Surface Ocean CO_2 variability and vulnerabilities). https://doi.org/10.1016/j.dsr2.2008.12.006

Dong, F., Li, Y., & Wang, B. (2017). Assessment of responses of tropical Pacific air–sea CO_2 flux to ENSO in 14 CMIP5 models. *Journal of Climate*, *30*(21), 8595–8613. https://doi.org/10.1175/JCLI-D-16-0543.1

Dong, F., Li, Y., Wang, B., Huang, W., Shi, Y., & Dong, W. (2016). Global air-sea CO_2 flux in 22 CMIP5 models: Multiyear mean and interannual variability. *Journal of Climate*, *29*(7), 2407–2431. https://doi.org/10.1175/jcli-d-14-00788.1

Emori, S., Taylor, K., Hewitson, B., Zermoglio, F., Juckes, M., Lautenschlager, M., & Stockhause, M. (2016). CMIP5 data provided at the IPCC data distribution centre [Computer software manual]. Fact Sheet of the Task Group on Data and Scenario Support for Impact and Climate Analysis (TGICA) of the Intergovernmental Panel on Climate Change (IPCC), *8*. https://doi.org/10.22033/ESGF/CMIP6.11298

Farneti, R., Stiz, A., & Ssebandeke, J. B. (2022). Improvements and persistent biases in the southeast tropical Atlantic in CMIP models. *npj Climate and Atmospheric Science*, *5*(1), 42. https://doi.org/10.1038/s41612-022-00264-4

Fay, A. R., Gregor, L., Landschützer, P., McKinley, G. A., Gruber, N., Gehlen, M., et al. (2021). Seaflux: Harmonization of air–sea CO_2 fluxes from surface pCO_2 data products using a standardized approach. *Earth System Science Data*, *13*(10), 4693–4710. https://doi.org/10.5194/essd-13-4693-2021

Feely, R. A., Takahashi, T., Wanninkhof, R., McPhaden, M. J., Cosca, C. E., Sutherland, S. C., & Carr, M.-E. (2006). Decadal variability of the air-sea CO_2 fluxes in the equatorial Pacific ocean. *Journal of Geophysical Research*, *111*(C8), C08S90. https://doi.org/10.1029/2005JC003129

Friedlingstein, P., Jones, M. W., O'Sullivan, M., Andrew, R. M., Bakker, D. C. E., Hauck, J., et al. (2022). Global carbon budget 2021. *Earth System Science Data*, *14*(4), 1917–2005. https://doi.org/10.5194/essd-14-1917-2022

Guo, H., John, J. G., Blanton, C., McHugh, C., Nikonov, S., Radhakrishnan, A., et al. (2018). NOAA-GFDL GFDL-CM4 model output historical [Dataset]. Earth System Grid Federation. https://doi.org/10.22033/ESGF/CMIP6.8594

Hajima, T., Abe, M., Arakawa, O., Suzuki, T., Komuro, Y., Ogura, T., et al. (2019). MIROC MIROC-ES2L model output prepared for CMIP6 CMIP historical [Dataset]. Earth System Grid Federation. https://doi.org/10.22033/ESGF/CMIP6.5602

Jin, C., Zhou, T., & Chen, X. (2019). Can CMIP5 Earth system models reproduce the interannual variability of air–sea CO_2 fluxes over the tropical Pacific ocean? *Journal of Climate*, *32*(8), 2261–2275. https://doi.org/10.1175/JCLI-D-18-0131.1

Jungclaus, J., Bittner, M., Wieners, K.-H., Wachsmann, F., Schupfner, M., Legutke, S., et al. (2019). MPI-M MPI-ESM1.2-HR model output prepared for CMIP6 CMIP historical [Dataset]. Earth System Grid Federation. https://doi.org/10.22033/ESGF/CMIP6.6594

Landschützer, P., Gruber, N., & Bakker, D. C. E. (2016). Decadal variations and trends of the global ocean carbon sink. *Global Biogeochemical Cycles*, *30*(10), 1396–1417. https://doi.org/10.1002/2015GB005359

Lauvset, S. K., Lange, N., Tanhua, T., Bittig, H. C., Olsen, A., Kozyr, A., et al. (2021). An updated version of the global interior ocean biogeochemical data product, GLODAPv2.2021. *Earth System Science Data*, *13*(12), 5565–5589. https://doi.org/10.5194/essd-13-5565-2021

Le Quéré, C., Orr, J. C., Monfray, P., Aumont, O., & Madec, G. (2000). Interannual variability of the oceanic sink of CO_2 from 1979 through 1997. *Global Biogeochemical Cycles*, *14*(4), 1247–1265. https://doi.org/10.1029/1999gb900049

Li, G., & Xie, S.-P. (2012). Origins of tropical-wide SST biases in CMIP multi-model ensembles. *Geophysical Research Letters*, *39*(22), L22703. https://doi.org/10.1029/2012GL053777

Liao, E., Resplandy, L., Liu, J., & Bowman, K. W. (2020). Amplification of the ocean carbon sink during El Niños: Role of poleward ekman transport and influence on atmospheric CO_2. *Global Biogeochemical Cycles*, *34*(9), e2020GB006574. https://doi.org/10.1029/2020GB006574

Long, M. C., Lindsay, K., Peacock, S., Moore, J. K., & Doney, S. C. (2013). Twentieth-century oceanic carbon uptake and storage in CESM1(BGC). *Journal of Climate*, *26*(18), 6775–6800. https://doi.org/10.1175/JCLI-D-12-00184.1

Lovenduski, N. S., Gruber, N., Doney, S. C., & Lima, I. D. (2007). Enhanced CO_2 outgassing in the southern ocean from a positive phase of the southern annular mode. *Global Biogeochemical Cycles*, *21*(2), GB2026. https://doi.org/10.1029/2006GB002900

McKinley, G. A., Fay, A. R., Lovenduski, N. S., & Pilcher, D. J. (2017). Natural variability and anthropogenic trends in the ocean carbon sink. *Annual Review of Marine Science*, *9*(1), 125–150. https://doi.org/10.1146/annurev-marine-010816-060529

McKinley, G. A., Follows, M. J., & Marshall, J. (2004). Mechanisms of air-sea CO_2 flux variability in the equatorial Pacific and the North Atlantic. *Global Biogeochemical Cycles*, *18*(2), GB2011. https://doi.org/10.1029/2003GB002179

Neubauer, D., Ferrachat, S., Siegenthaler-Le Drian, C., Stoll, J., Folini, D. S., Tegen, I., et al. (2019). HAMMOZ-Consortium MPI-ESM1.2-HAM model output prepared for CMIP6 CMIP historical [Dataset]. Earth System Grid Federation. https://doi.org/10.22033/ESGF/CMIP6.5016

Rayner, N. A., Parker, D. E., Horton, E. B., Folland, C. K., Alexander, L. V., Rowell, D. P., & Kaplan, A. (2003). Global analyses of sea surface temperature, sea ice, and night marine air temperature since the late nineteenth century. *Journal of Geophysical Research*, *108*(D14), 4407. https://doi.org/10.1029/2002JD002670

Resplandy, L., Séférian, R., & Bopp, L. (2015). Natural variability of CO_2 and O_2 fluxes: What can we learn from centuries-long climate models simulations? *Journal of Geophysical Research: Oceans*, *120*(1), 384–404. https://doi.org/10.1002/2014JC010463

Rödenbeck, C., Bakker, D. C. E., Metzl, N., Olsen, A., Sabine, C., Cassar, N., et al. (2014). Interannual sea–air CO_2 flux variability from an observation-driven ocean mixed-layer scheme. *Biogeosciences*, *11*(17), 4599–4613. https://doi.org/10.5194/bg-11-4599-2014

Sarmiento, J. L., & Gruber, N. (2006). *Ocean biogeochemical dynamics*. Princeton University Press.

Seager, R., Cane, M., Henderson, N., Lee, D. E., Abernathey, R., & Zhang, H. (2019). Strengthening tropical Pacific zonal sea surface temperature gradient consistent with rising greenhouse gases. *Nature Climate Change*, *9*(7), 517–522. https://doi.org/10.1038/s41558-019-0505-x

Séférian, R. (2018). CNRM-CERFACS CNRM-ESM2-1 model output prepared for CMIP6 CMIP historical [Dataset]. Earth System Grid Federation. https://doi.org/10.22033/ESGF/CMIP6.4068

Séférian, R., Berthet, S., Yool, A., Palmieri, J., Bopp, L., Tagliabue, A., et al. (2020). Tracking improvement in simulated marine biogeochemistry between CMIP5 and CMIP6. *Current Climate Change Reports*, *6*(3), 95–119. https://doi.org/10.1007/s40641-020-00160-0

Seland, Y., Bentsen, M., Oliviè, D. J. L., Toniazzo, T., Gjermundsen, A., Graff, L. S., et al. (2019). NCC NorESM2-LM model output prepared for CMIP6 CMIP historical [Dataset]. Earth System Grid Federation. https://doi.org/10.22033/ESGF/CMIP6.8036

Sutton, A. J., Feely, R. A., Sabine, C. L., McPhaden, M. J., Takahashi, T., Chavez, F. P., et al. (2014). Natural variability and anthropogenic change in equatorial Pacific surface ocean pCO_2 and pH. *Global Biogeochemical Cycles*, *28*(2), 131–145. https://doi.org/10.1002/2013GB004679

Swart, N. C., Cole, J. N., Kharin, V. V., Lazare, M., Scinocca, J. F., Gillett, N. P., et al. (2019a). CCCma CanESM5 model output prepared for CMIP6 CMIP historical [Dataset]. Earth System Grid Federation. https://doi.org/10.22033/ESGF/CMIP6.3610

Swart, N. C., Cole, J. N., Kharin, V. V., Lazare, M., Scinocca, J. F., Gillett, N. P., et al. (2019b). CCCma CanESM5-CanOE model output prepared for CMIP6 CMIP historical [Dataset]. Earth System Grid Federation. https://doi.org/10.22033/ESGF/CMIP6.10260

Takahashi, T., Olafsson, J., Goddard, J. G., Chipman, D. W., & Sutherland, S. C. (1993). Seasonal variation of CO_2 and nutrients in the high-latitude surface oceans: A comparative study. *Global Biogeochemical Cycles*, *7*(4), 843–878. https://doi.org/10.1029/93GB02263

Takahashi, T., Sutherland, S. C., Sweeney, C., Poisson, A., Metzl, N., Tilbrook, B., et al. (2002). Global sea–air CO_2 flux based on climatological surface ocean pCO_2, and seasonal biological and temperature effects. *Deep Sea Research Part II: Topical Studies in Oceanography*, *49*(9), 1601–1622. (The southern ocean I: Climatic changes in the cycle of carbon in the southern ocean). https://doi.org/10.1016/S0967-0645(02)00003-6

Takahashi, T., Sutherland, S. C., Wanninkhof, R., Sweeney, C., Feely, R. A., Chipman, D. W., et al. (2009). Climatological mean and decadal change in surface ocean pCO_2, and net sea–air CO_2 flux over the global oceans. *Deep Sea Research Part II: Topical Studies in Oceanography*, *56*(8), 554–577. (Surface ocean CO_2 variability and vulnerabilities). https://doi.org/10.1016/j.dsr2.2008.12.009

Taylor, K. E., Stouffer, R. J., & Meehl, G. A. (2012). An overview of CMIP5 and the experiment design. *Bulletin of the American Meteorological Society*, *93*(4), 485–498. https://doi.org/10.1175/bams-d-11-00094.1

Vaittinada Ayar, P., Tjiputra, J., Bopp, L., Christian, J. R., Ilyina, T., Krasting, J. P., et al. (2022). Contrasting projection of the ENSO-driven CO_2 flux variability in the equatorial Pacific under high warming scenario. *Earth System Dynamics Discussions*, *13*(3), 1–31. https://doi.org/10.5194/esd-2022-12

Wanninkhof, R. (2014). Relationship between wind speed and gas exchange over the ocean revisited. *Limnology and Oceanography: Methods*, *12*(6), 351–362. https://doi.org/10.4319/lom.2014.12.351

Wieners, K.-H., Giorgetta, M., Jungclaus, J., Reick, C., Esch, M., Bittner, M., et al. (2019). MPI-M MPI-ESM1.2-LR model output prepared for CMIP6 CMIP historical [Dataset]. Earth System Grid Federation. https://doi.org/10.22033/ESGF/CMIP6.6595

Yukimoto, S., Koshiro, T., Kawai, H., Oshima, N., Yoshida, K., Urakawa, S., et al. (2019). MRI MRI-ESM2.0 model output prepared for CMIP6 CMIP historical [Dataset]. Earth System Grid Federation. https://doi.org/10.22033/ESGF/CMIP6.6842

Ziehn, T., Chamberlain, M., Lenton, A., Law, R., Bodman, R., Dix, M., et al. (2019). CSIRO ACCESS-ESM1.5 model output prepared for CMIP6 CMIP historical [Dataset]. Earth System Grid Federation. https://doi.org/10.22033/ESGF/CMIP6.4272

Zuo, H., Balmaseda, M. A., Tietsche, S., Mogensen, K., & Mayer, M. (2019). The ECMWF operational ensemble reanalysis–analysis system for ocean and sea ice: A description of the system and assessment. *Ocean Science*, *15*(3), 779–808. https://doi.org/10.5194/os-15-779-2019